Article

Developmental Cell

Liquid-like condensates that bind actin promote assembly and bundling of actin filaments

Graphical abstract

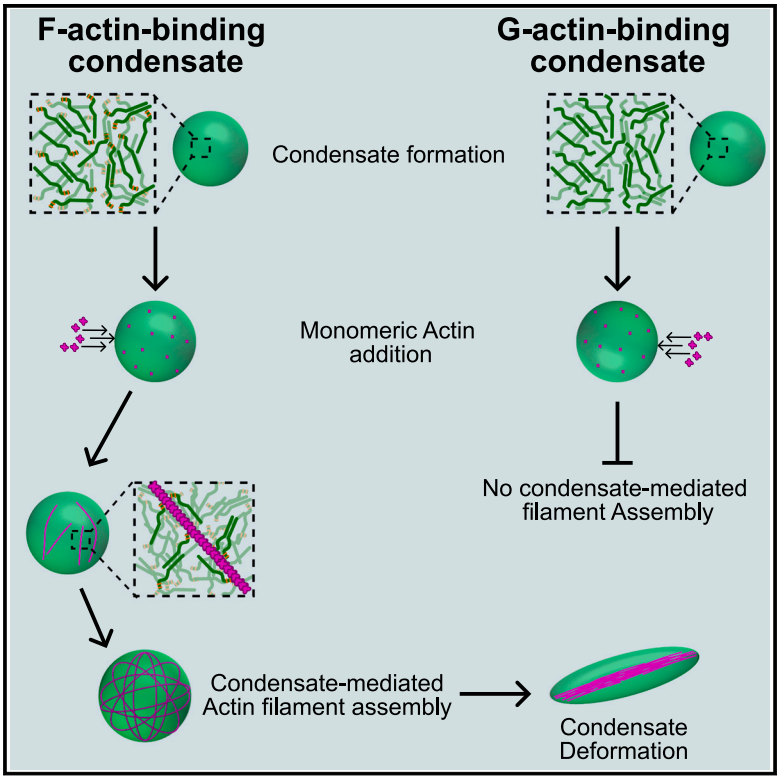

Highlights

- Cytoskeletal accessory proteins VASP and Lamellipodin form liquid-like condensates
- Condensates facilitate actin assembly, even in the absence of actin polymerases
- Multivalent actin binding by condensates is sufficient for actin filament bundling
- The addition of F-actin binding to condensate proteins facilitates actin assembly

Authors

Caleb Walker, Aravind Chandrasekaran, Daniel Mansour, ..., Eileen M. Lafer, Padmini Rangamani, Jeanne C. Stachowiak

Correspondence

prangamani@ucsd.edu (P.R.), jcstach@austin.utexas.edu (J.C.S.)

In brief

While diverse actin-interacting proteins have the potential to form protein condensates, the role of condensates during the assembly of the cytoskeleton remains unclear. Walker et al. report that flexible, multivalent interactions between condensate proteins and actin filaments have an inherent capacity to promote the assembly and bundling of actin filaments.

Walker et al., 2025, Developmental Cell *60*, 1550–1567
June 9, 2025
https://doi.org/10.1016/j.devcel.2025.01.012

CellPress

CellPress

Developmental Cell

Article

Liquid-like condensates that bind actin promote assembly and bundling of actin filaments

Caleb Walker,[1] Aravind Chandrasekaran,[2,7] Daniel Mansour,[2,7] Kristin Graham,[3] Andrea Torres,[1] Liping Wang,[4] Eileen M. Lafer,[4] Padmini Rangamani,[2,5,*] and Jeanne C. Stachowiak[1,6,8,*]

[1]Biomedical Engineering, The University of Texas at Austin, Austin, TX, USA
[2]Department of Mechanical and Aerospace Engineering, University of California, San Diego, La Jolla, CA, USA
[3]Cell and Molecular Biology, The University of Texas at Austin, Austin, TX, USA
[4]Department of Biochemistry and Structural Biology, University of Texas Health Science Center at San Antonio, San Antonio, TX, USA
[5]Department of Pharmacology, University of California, San Diego School of Medicine, La Jolla, CA, USA
[6]Chemical Engineering, The University of Texas at Austin, Austin, TX, USA
[7]These authors contributed equally
[8]Lead contact
*Correspondence: prangamani@ucsd.edu (P.R.), jcstach@austin.utexas.edu (J.C.S.)
https://doi.org/10.1016/j.devcel.2025.01.012

SUMMARY

Biomolecular condensates perform diverse physiological functions. Previous work showed that VASP, a processive actin polymerase, forms condensates that assemble and bundle actin. Here, we show that this behavior does not require proteins with specific polymerase activity. Specifically, condensates composed of Lamellipodin, a protein that binds actin but is not an actin polymerase, were also capable of assembling actin filaments. To probe the minimum requirements for condensate-mediated actin bundling, we developed an agent-based computational model. Guided by its predictions, we hypothesized that any condensate-forming protein that binds filamentous actin could bundle filaments through multivalent crosslinking. To test this, we added a filamentous-actin-binding motif to Eps15, a condensate-forming protein that does not normally bind actin. The resulting chimera formed condensates that facilitated efficient assembly and bundling of actin filaments. Collectively, these findings broaden the family of proteins that could organize cytoskeletal filaments to include any filamentous-actin-binding protein that participates in protein condensation.

INTRODUCTION

The actin cytoskeleton forms filament networks that play a critical role in cell motility, endocytosis, and adhesion.[1–4] A family of actin accessory proteins collectively determines filament elongation rate, length, and arrangement into networks.[5–7] Several cytoskeletal accessory proteins have recently been shown to form condensates via liquid-liquid phase separation (LLPS), a phenomenon in which biomolecules self-assemble into a liquid-like condensed phase surrounded by a dilute phase.[8–10] Interestingly, these biomolecular condensates can nucleate the assembly of cytoskeletal filaments. For example, condensates consisting of proteins from the T cell receptor phosphorylation cascade are capable of concentrating and assembling actin filaments.[11] Similarly, condensates formed from the *C. elegans* tubulin polymerase SPD-5 can nucleate microtubule aster formation in the presence of the microtubule-stabilizing proteins TPXL-1 and ZYG-9.[12] Building on these findings, we recently showed that condensates consisting of the actin polymerase VASP can assemble and bundle actin filaments.[13] As a homotetramer with a high degree of intrinsic disorder, VASP has key hallmarks of proteins that form biomolecular condensates.[14–16] As actin filaments elongated inside VASP condensates of micrometer diameter, actin filaments, which have a persistence length of 10–20 micrometers,[17] accumulated at the inner surfaces of condensates to minimize filament curvature. This partitioning led to the assembly of a peripheral, ring-like bundle of actin within condensates. As actin filaments continued to elongate, an increasing number of filaments joined this ring, increasing its rigidity. When the rigidity of the actin ring overcame the surface tension of the VASP condensate, the filaments within the ring began to straighten, deforming the initially spherical VASP condensates into elliptical and rod-like shapes filled with parallel bundles of actin filaments.[13,18]

In cells, VASP works together with multiple other cytoskeletal accessory proteins to facilitate the assembly and bundling of actin filaments. Each monomer of VASP consists of an N-terminal Enabled/VASP homology 1 (EVH1) domain, which binds to short proline-rich sequences in its binding partners. The EVH1 domain is followed by VASP's central proline-rich region and then by an EVH2 domain through which VASP binds and facilitates filament elongation. Finally, VASP contains a C-terminal tetramerization domain.[14–16] The EVH1 domain of VASP interacts with proline-rich repeats in multiple cytoskeletal accessory

proteins, many of which are native multimers with a high degree of intrinsic disorder.[19–22] These features suggest that VASP's binding partners could reinforce its condensation, helping to build a more stable protein network that is capable of assembling actin filaments and controlling the morphology of the resulting filament network. As one example, our recent work showed that the addition of Arp2/3, which nucleates the assembly of branched actin networks, to VASP condensates results in aster-shaped structures.[23] Another VASP binding partner is Lamellipodin (Lpd), which has been shown to interact with VASP in cytoskeletal protrusions such as lamellipodia and filopodia.[20,24–27] Lamellipodin dimerizes via an N-terminal coiled-coil domain,[28] which is followed by a Ras-associating and Pleckstrin homology domain (RA-PH), which allows Lamellipodin to localize to the plasma membrane via lipid binding.[29] After the RA-PH domain, Lamellipodin's C terminus is proline-rich and highly disordered. It is within this C-terminal disordered region that Lamellipodin contains several proline-rich regions that include multiple EVH1 binding sequences.[20,26] While Lamellipodin binds actin filaments,[25,30] it lacks actin polymerase activity.[25] This observation suggests that Lamellipodin recruits and clusters other cytoskeletal accessory proteins, such as VASP, during membrane remodeling events.[25] Interestingly, at the leading edge of motile cells, Lamellipodin and VASP form dynamic clusters that undergo dynamic fission and fusion events.[24,25] This observation, in addition to the recent finding that VASP and Lamellipodin co-partition into protein condensates,[31] suggests that the two proteins form a flexible, liquid-like network.

Here, we asked how interactions between VASP and Lamellipodin impact the ability of protein condensates to assemble and bundle actin filaments. We began by characterizing the ability of Lamellipodin to form liquid-like condensates *in vitro* and to stabilize the assembly of VASP condensates. When actin was added to these condensates, it formed filaments and bundles, deforming the condensates into rod-like structures, similar to our previous observations with condensates consisting of VASP alone.[13] Surprisingly, we found that condensates consisting of Lamellipodin alone can also assemble and bundle actin filaments, despite Lamellipodin's reported lack of polymerase activity. How does the formation of protein condensates confer this capacity upon Lamellipodin? Multivalent binding to actin filaments is thought to underlie the ability of specialized actin polymerases, such as formins and members of the ENA/VASP family, to stabilize filament bundles and add monomers to growing filament nuclei.[7,14,15,32,33] Therefore, one possible explanation is that the condensate environment promotes multivalent interactions between Lamellipodin and actin. To investigate the potential contribution of protein condensates to actin bundling, we developed an agent-based model of filament rearrangement within spherical containers that mimic protein condensates. In this context, we examined the ability of actin accessory proteins, such as VASP and Lamellipodin, to bundle actin filaments. This model predicted that any actin-binding protein that forms a multivalent complex, either stably or dynamically, is sufficient to bundle actin filaments. To test this hypothesis, we formed protein condensates of Eps15, an endocytic protein lacking known interactions with actin.[34–36] When we added the actin-binding motif, Lifeact, to the C terminus of this protein, the resulting chimera formed condensates that spontaneously assembled and bundled actin filaments. Collectively, these results suggest that filament assembly and bundling are emergent properties of liquid-like protein condensates that bind actin filaments. Given that many actin-interacting proteins are now thought to participate in protein condensation,[11,13,23,37–41] our results suggest a general principle of actin organization through multivalent interactions.

RESULTS

Lamellipodin phase separates into liquid-like condensates

As a native dimer with a high degree of intrinsic disorder, Lamellipodin has key hallmarks of the ability to form biomolecular condensates.[8,9] In particular, its largely disordered C-terminal region (residues 850–1,250) contains twenty-seven negatively charged residues (aspartate and glutamate) and forty-four positively charged residues (lysine and arginine)[20,25] suggesting a strong potential for intra and intermolecular electrostatic interactions. Further, the same region contains ninety-nine proline residues, which tend to increase chain rigidity, contributing to intrinsic disorder and phase separation.[42,43] To study the potential of Lamellipodin to phase separate *in vitro*, we used a minimal model of the full-length protein for ease of expression and purification, as has been previously reported.[24,25] This minimal protein, which we will refer to as mini-Lpd, consisted of an N-terminal GFP domain, followed by a dimerizing leucine zipper motif to imitate native dimerization, and ending with a large portion of the C-terminal disordered region of Lamellipodin, specifically residues 850–1,250 (Figures 1A and 1B). While mini-Lpd lacks the N-terminal portion of Lamellipodin, sequence analysis and algorithms for predicting phase separation suggest that the portions of the full-length protein that are omitted are likely to reinforce, rather than inhibit, phase separation (Figures S1A and S1B).

To test the ability of mini-Lpd to form phase-separated protein condensates, we mixed 5–15 μM mini-Lpd with 3% (w/v) Poly (ethylene glycol) (PEG) 8000. PEG is commonly added in the study of LLPS to mimic the crowded environment in the cell cytoplasm.[44–46] Upon the addition of PEG, mini-Lpd formed spherical protein condensates with diameters in the micrometer range, which increased in size with increasing protein concentration (Figure 1C). These condensates fused and rerounded upon contact within a second (Figure 1D), suggesting liquid-like behavior.[10,47] Additionally, mini-Lpd condensates recovered rapidly after photobleaching, indicating dynamic molecular exchange (Figures 1E and 1F). The average size of condensates, as well as protein partitioning into them, decreased substantially as ionic strength increased, suggesting that electrostatic interactions, which are screened at high ionic strength, stabilize condensates (Figures 1G–1I). Additionally, by locally concentrating mini-Lpd on membrane substrates, we observed phase separation at much lower concentrations than were used to form condensates *in vitro*, approximately 50 nM (Figure S1E). Similarly, a recent study reported co-phase separation of VASP and Lamellipodin at low concentrations on membrane surfaces.[48] As both Lamellipodin and VASP function in membrane-localized processes, we expect that local concentration on membrane surfaces facilitates their condensation at endogenous expression levels, likely lower than the concentrations used for phase separation *in vitro*.

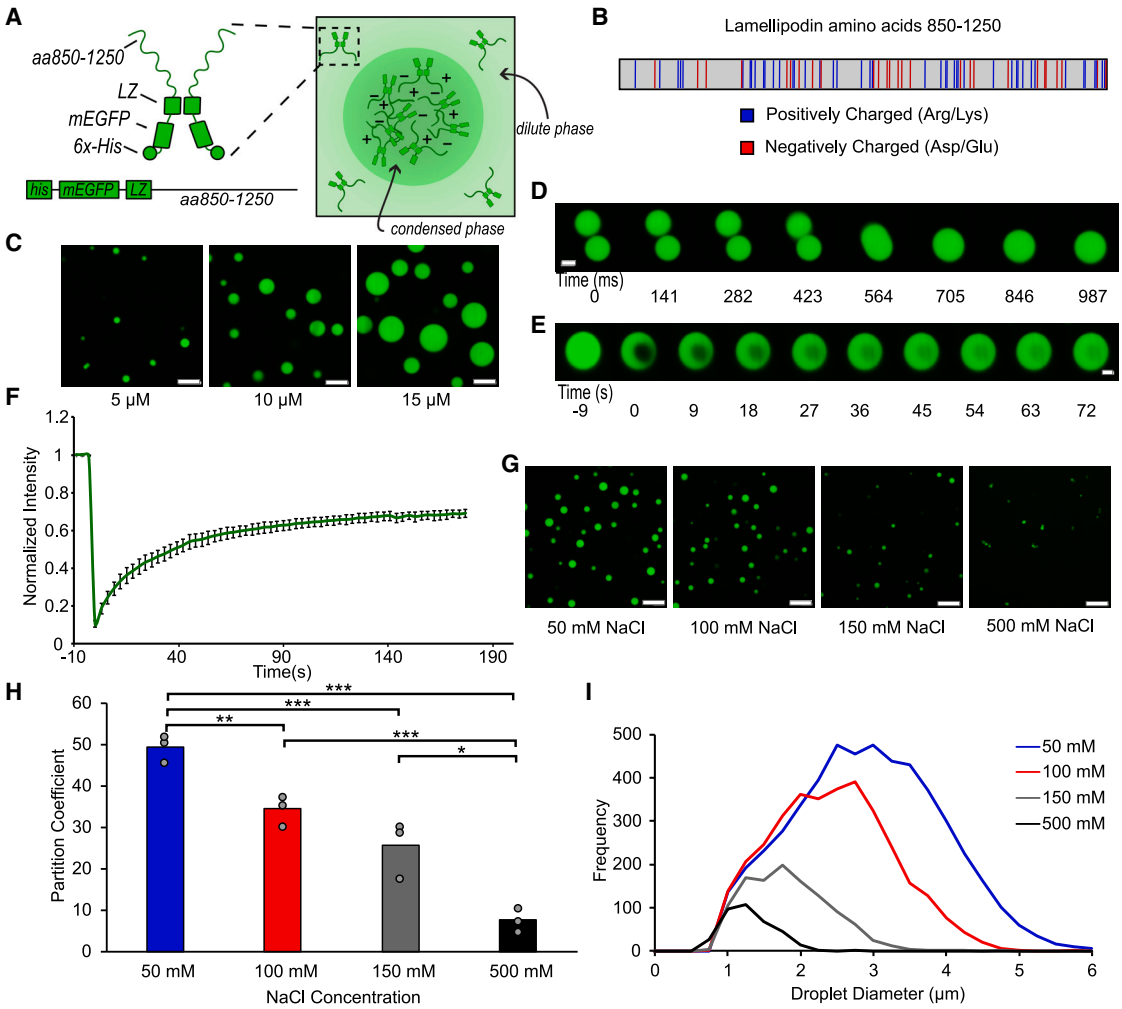

Figure 1. A minimal version of Lamellipodin phase separates into liquid-like condensates

(A) Left: schematic depicting domains of mini-Lpd (LZ, leucine zipper). Right: schematic depicting condensate formation.

(B) Amino acid sequence of amino acids 850–1,250 of Lamellipodin with positively charged (blue) and negatively charged (red) amino acids highlighted.

(C) Condensates formed by mini-Lpd at increasing protein concentrations in a buffer containing 20 mM Tris (pH 7.4), 150 mM NaCl, 5 mM tris(2-carboxyethyl) phosphine (TCEP), and 3% w/v PEG. Scale bars are 5 μm.

(D) Time course of condensate fusion event for 10 μM mini-Lpd in buffer containing 20 mM Tris (pH 7.4), 50 mM NaCl, and 5 mM TCEP. Scale bar, 2 μm.

(E) Representative images of fluorescence recovery after photobleaching of a mini-Lpd condensate. Scale bar, 2 μm.

(F) Plot of average fluorescence recovery ± SD after photobleaching for mini-Lpd condensates across $n = 6$ independent samples.

(G) Condensate of 10 μM mini-Lpd formed in buffers with increasing ionic strength. Scale bars are 5 μm.

(H) Quantification of 10 μM mini-Lpd partitioning into condensates under the conditions shown in (G). Partition coefficient is defined as the ratio of protein intensity inside the condensates to that in the bulk solution. Bars represent the average across three independent experiments. Overlaid gray circles denote the averages for each replicate. One asterisk denotes $p < 0.05$, two asterisks denote $p < 0.01$, and three asterisks denote $p < 0.001$ using an unpaired, two-tailed t test on the means of the replicates $n = 3$.

(I) Distribution of condensate diameters for the conditions shown in (G) across three separate replicates for each condition.

Interactions between Lamellipodin and VASP mutually stabilize protein condensation

Having established that mini-Lpd can undergo LLPS, we next investigated the potential impact of mini-Lpd on the phase separation of VASP. Our previous work showed that VASP forms liquid-like condensates across a range of protein concentrations and ionic strengths when 3% (w/v) PEG 8000 is used as a crowding agent.[13] We hypothesized that adding mini-Lpd could strengthen the VASP network by forming multivalent interactions between the multiple proline-rich motifs in each Lamellipodin protein, which are recognized by the four EVH1 domains in the VASP tetramer (Figure 2A). To test this idea, we first confirmed that neither VASP nor mini-Lpd were able to form condensates in the absence of PEG (Figure 2B). We then combined mini-Lpd and VASP at increasing ratios, keeping the total protein concentration constant at 30 μM. Beginning with pure mini-Lpd, we gradually increased the VASP concentration from 7.5 to 22.5 μM, finding a range of ratios from 3:1 mini-Lpd:VASP to 1:3 mini-Lpd:VASP for which condensate formation was observed in the absence of PEG (Figures 2C and 2D). Condensates of mini-Lpd and VASP that

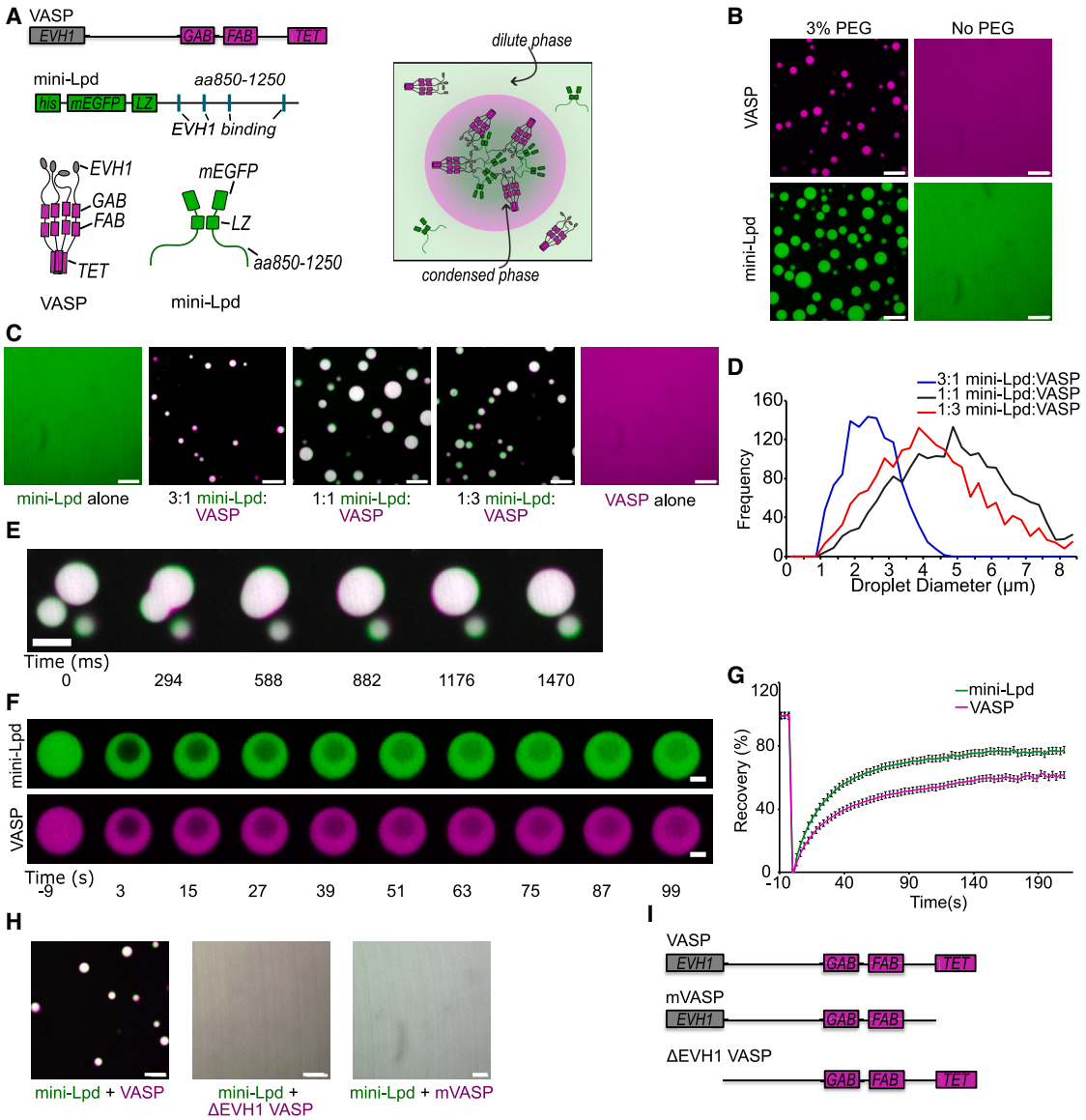

Figure 2. Interactions between Lamellipodin and VASP mutually stabilize protein condensation

(A) Top: schematic of domain organization in a VASP monomer (GAB, G-actin-binding site; FAB, F-actin-binding site; TET, tetramerization domain) and a mini-Lpd monomer (LZ, leucine zipper dimerization motif). Bottom: schematic of VASP tetramer, mini-Lpd dimer. Right: schematic depicting mini-Lpd and VASP co-partitioning into a condensate.

(B) Condensates form upon the inclusion of 3% w/v PEG in solution for both 20 μM VASP (magenta) and 20 μM mini-Lpd (green); however, neither protein forms condensates in buffer lacking PEG. Scale bars, 5 μm.

(C) Panels showing representative images of mini-Lpd + VASP condensates formed at various mini-Lpd to VASP ratios. Scale bars, 5 μm.

(D) Distribution of condensate diameters for each condition in (C).

(E) Time course of a condensate fusion event between mini-Lpd (green) and VASP (magenta) condensates. Scale bar, 2 μm.

(F) Representative images of fluorescence recovery after photobleaching of a mini-Lpd (green) and VASP (magenta) condensate. Scale bars, 2 μm.

(G) Plot of average fluorescence recovery, ±SD, after photobleaching for mini-Lpd and VASP condensates formed in the absence of PEG across $n = 9$ independent samples.

(H) Mini-Lpd added to the respective VASP mutant in a 1:1 ratio to test for condensate formation in the absence of PEG. Left, mini-Lpd (green) and VASP (magenta); middle, mini-Lpd (green) and VASPΔEVH1 (magenta); right, mini-Lpd (green) and monomeric VASP (mVASP) (magenta). Scale bars, 5 μm.

(I) Diagrams depict domain structures of VASP mutants. All experiments were performed in a buffer containing 20 mM Tris (pH 7.4), 150 mM NaCl, and 5 mM TCEP in the absence of PEG, except where noted in (B) where 3% (w/v) PEG was included.

formed in the absence of PEG retained liquid-like properties, merging and rerounding upon contact in less than a second (Figure 2E) and recovering rapidly after photobleaching (Figures 2F and 2G). To test the dependency of these condensates on multivalent contacts between VASP and mini-Lpd, we evaluated mutants of VASP that would be expected to inhibit such contacts. These included a

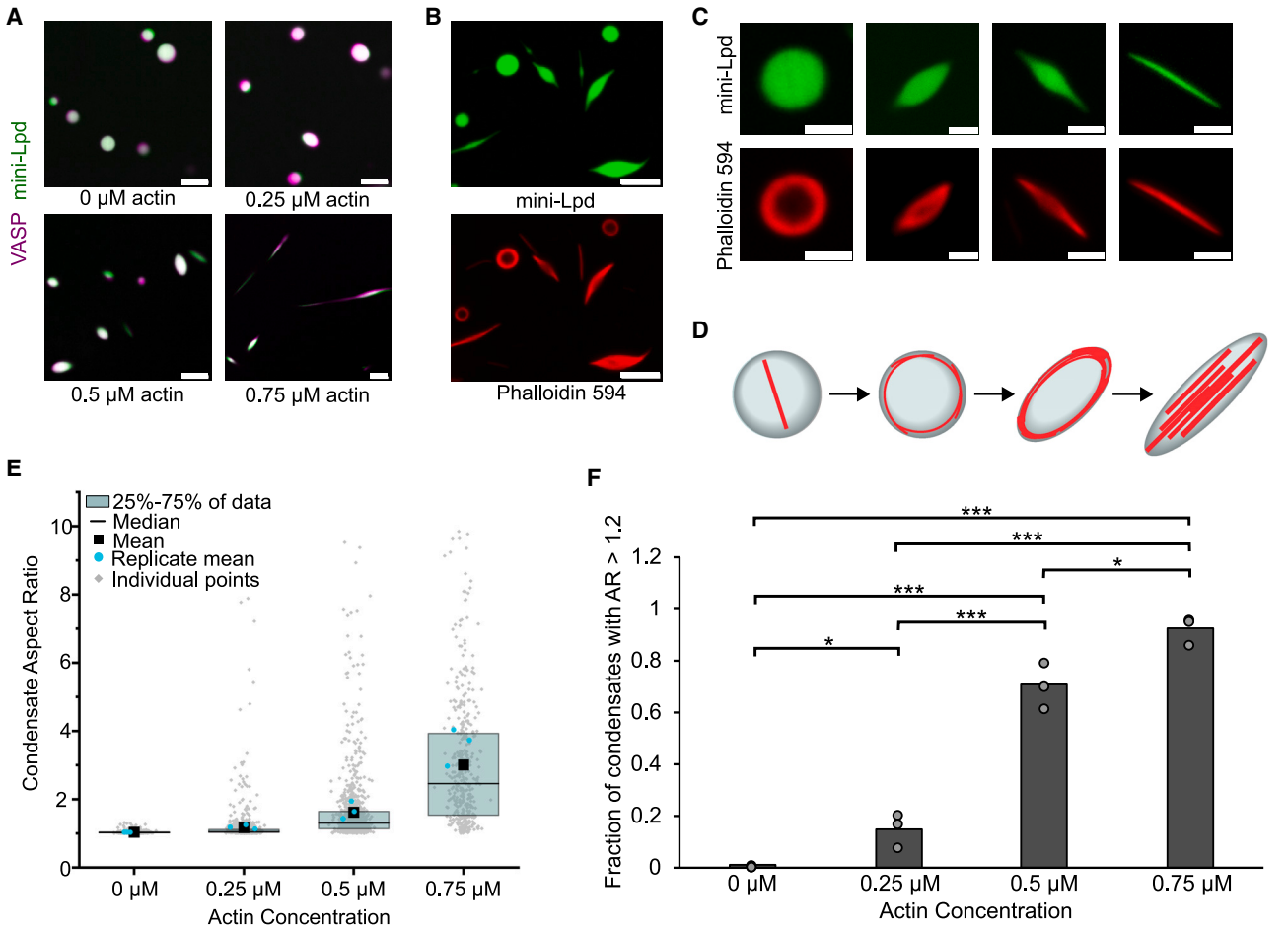

Figure 3. Condensates of VASP and mini-Lpd assemble and bundle actin in the absence of crowding agents

(A) Condensates formed from 5 μM mini-Lpd (green) and 10 μM VASP (magenta) are increasingly deformed with the addition of increasing concentrations of G-actin (unlabeled). Scale bars, 5 μm.

(B) Phalloidin-iFluor-594 (red) staining of mini-Lpd (green) and VASP (unlabeled) condensates with 0.5 μM monomeric G-actin displaying rings and rods of actin filaments within the protein condensates. Scale bars, 5 μm.

(C) Representative confocal images depicting the progression of condensate deformation as actin forms filaments and bundles within the protein condensates. Scale bars, 2 μm.

(D) Cartoon depicting the mechanism of actin assembly within protein condensates and subsequent condensate deformation.

(E) Distribution of condensate aspect ratios across the conditions in (A), with at least 400 condensates analyzed for each condition. In the 0.75 μM actin condition, values for aspect ratios above 10, corresponding to 4.8% of the data, are not displayed to better visualize distributions for all conditions.

(F) Quantification of the fraction of elongated protein condensates, defined as condensates with aspect ratios >1.2, across the conditions in (A). Data are mean across three independent experiments with at least 400 condensates analyzed per condition. Overlaid gray circles denote the means of each replicate. One asterisk denotes $p < 0.05$, and three asterisks denote $p < 0.001$ using an unpaired, two-tailed t test on the means of the replicates $n = 3$. All experiments were performed in a buffer containing 20 mM Tris (pH 7.4), 150 mM NaCl, and 5 mM TCEP in the absence of PEG.

monomeric version of VASP (mVASP), which lacked the tetramerization domain, and a version of VASP lacking the EVH1 domain, ΔEVH1-VASP. Both proteins failed to form condensates upon the addition of mini-Lpd at concentrations that drove condensation of wild-type (WT) VASP. These data suggest that multivalent contacts between VASP and mini-Lpd are essential to the co-condensation of the two proteins (Figures 2H and 2I).

Condensates of VASP and mini-Lpd assemble and bundle actin

Next, we evaluated the ability of VASP/mini-Lpd condensates to assemble and bundle actin filaments. We added increasing concentrations of monomeric actin (G-actin) to protein condensates formed from mini-Lpd and VASP in the absence of PEG. Importantly, just as was seen previously with VASP condensates alone,[13,23] the buffers used in condensate experiments did not facilitate spontaneous actin assembly (Figure S2A). As the concentration of actin increased, the protein condensates began to deform, taking on increasingly elongated shapes (Figure 3A). We confirmed that actin assembled within the condensates by phalloidin staining, which specifically binds to filamentous actin (Figure 3B), permitting us to visualize the gradual deformation of condensations from initially spherical shapes to ellipsoids and finally to rod-like geometries (Figures 3C and 3D). These

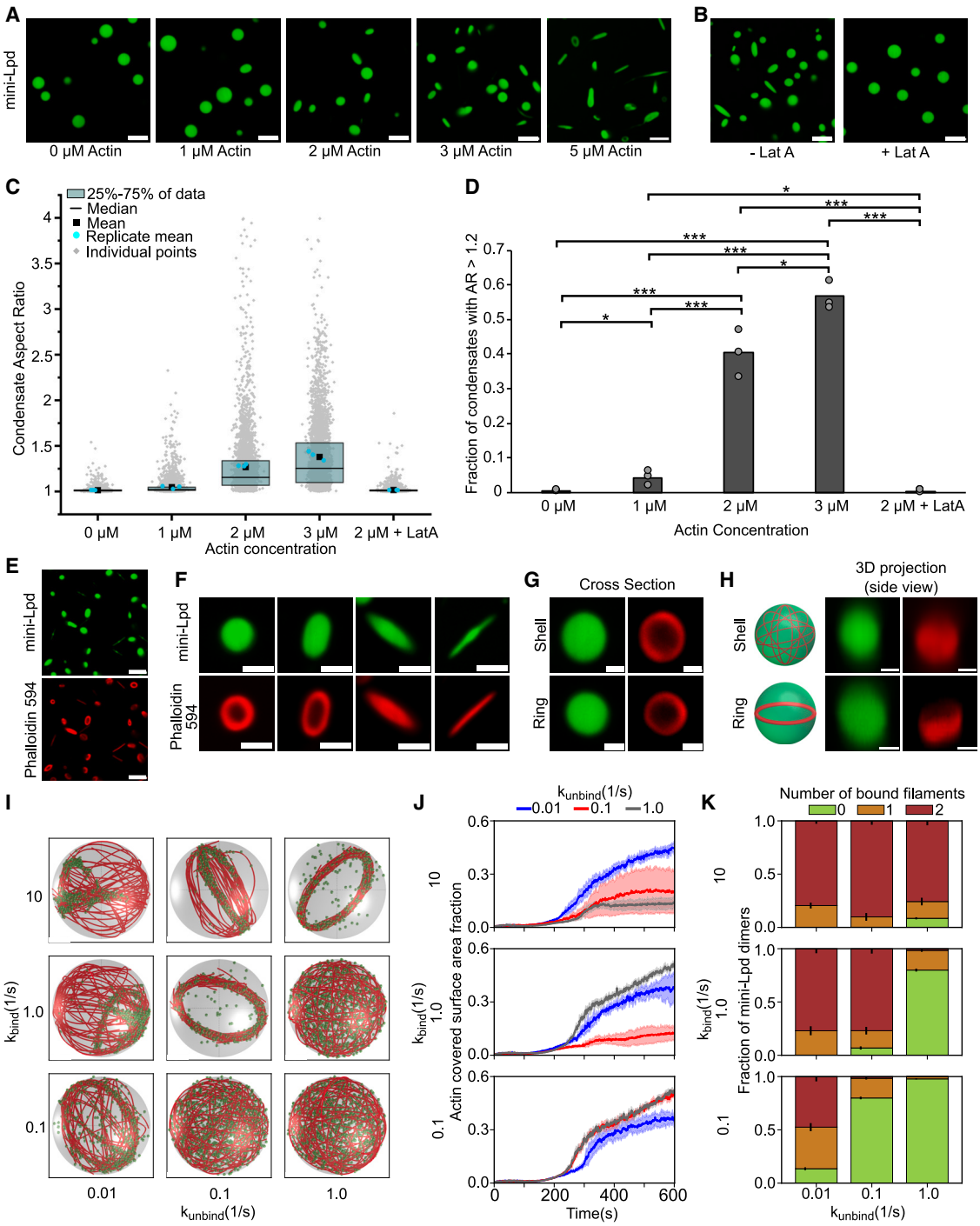

Figure 4. Condensates of mini-Lpd assemble and bundle actin filaments

(A) The addition of actin at increasing concentrations to condensates formed from 5 μM mini-Lpd (green) results in increasingly deformed protein condensates. Scale bars, 5 μm.

(B) Pretreatment of mini-Lpd condensates with 5 μM latrunculin A (LatA) prior to G-actin addition inhibits actin filament assembly and results in spherical condensates. Scale bars, 5 μm.

(C) Distribution of condensate aspect ratios across the conditions in (A), with at least 1,000 condensates analyzed for each condition.

(D) Quantification of the fraction of high-aspect-ratio protein condensates, defined as condensates with aspect ratios >1.2, across the conditions in (A). Data are mean across three independent experiments with at least 1,000 condensates analyzed per condition. Overlaid gray circles denote the means of each replicate. One asterisk denotes $p < 0.05$, two asterisks denote $p < 0.01$, and three asterisks denote $p < 0.001$ using an unpaired, two-tailed t test on the means of the replicates, $n = 3$.

(legend continued on next page)

morphological changes are in line with our previous observations with condensates consisting of VASP alone,[13] where time-lapse imaging showed distinct sphere-to-rod transitions and elongation of deformed condensates over time (Figures S2C–S2G). Phalloidin staining also showed that actin filaments with lengths greater than the optical diffraction limit were only found within the condensates, not in the surrounding solution (Figure S2B). However, these data do not rule out the possibility that small filament nuclei may form in the surrounding solution and partition into condensates where they are subsequently elongated. For condensates consisting of VASP and mini-Lpd, the aspect ratio (longest dimension divided by shortest dimension) of the condensates increased with increasing actin concentration, as did the fraction of condensates with aspect ratios above a threshold value of 1.2 (Figures 3E and 3F). To test whether condensates of mini-Lpd and VASP retained liquid-like properties during actin assembly, deformed condensates were subjected to photobleaching and were found to recover rapidly (Figures S3A and S3B). As expected for stably assembled filaments, the actin signal recovered minimally after photobleaching. Additionally, elongated condensates "zippered" together quickly upon contact, as expected for filaments wetted by a liquid-like phase (Figure S3J).

Condensates of mini-Lpd assemble and bundle actin filaments in the absence of VASP

VASP is a well-characterized actin polymerase and bundling protein.[14,15,49] By contrast, Lamellipodin binds actin filaments but fails to increase their rate of barbed end elongation.[25] Therefore we expected that condensates formed from mini-Lpd alone (Figure 1) would fail to assemble and bundle actin filaments. To test this assumption, we added monomeric actin to preformed condensates of mini-Lpd. Surprisingly, we found that the condensates deformed upon actin addition, suggesting that actin was assembling into filaments and bundles inside the condensates (Figure 4A). Latrunculin A[50] inhibited both filament assembly and condensate deformation, establishing that actin filament assembly led to deformation of mini-Lpd condensates (Figure 4B). Just as with condensates of mini-Lpd and VASP, condensates of mini-Lpd alone retained liquid-like properties after actin addition (Figures S3C, S3D, and S3I). Increasing the concentration of actin added to mini-Lpd condensates resulted in higher aspect ratios and a higher fraction of condensates with an aspect ratio above 1.2 (Figures 4C and 4D). Phalloidin staining revealed that filamentous actin bundles were present inside mini-Lpd condensates as they deformed from spherical to rod-like structures (Figures 4E and 4F), including shells and rings of actin as was seen in previous work with VASP alone (Figures 4G and 4H).[13] Owing to these surprising results, we decided to perform simulations aimed at determining the key physical requirements for filament bundling by protein condensates.

Agent-based simulations predict that multivalent crosslinking of actin filaments facilitates condensate-mediated bundling

Our previous work showed that the formation of a ring-like bundle of actin filaments within condensates is a critical step along the path to condensate deformation by actin.[13,18] We sought to understand how actin-binding proteins such as VASP and Lamellipodin impact this transition. In previous work, we used an agent-based model to examine the geometrical arrangement of growing actin filaments in the presence of VASP, which was represented as a tetrameric actin-binding protein. When placed inside a spherical container to mimic the condensate geometry, VASP promoted the assembly of actin filaments into ring-like bundles.[18] These simulations revealed that VASP can form bundles of actin in kinetic regimes characterized by a slightly higher rate of VASP-actin binding than unbinding.[18] However, when the rate of unbinding was higher than the rate of binding, the actin filaments failed to form a ring, remaining in a shell-like arrangement. Here, we adapted this model to investigate whether a bivalent actin-binding protein, similar to Lamellipodin, could also facilitate the formation of actin rings in the condensate environment, where the protein is locally concentrated in the presence of actin filaments (Figure S4). Our simulations revealed a kinetic regime in which bivalent actin-binding proteins drive actin filaments to undergo a shell-to-ring transition (Figures 4I–4K). To monitor this transition in our simulations, we quantified two metrics.[18] First, we observed that the presence of bivalent actin crosslinkers causes a reduction in the fraction of the inner condensate surface occupied by filaments, as would be expected for a shell-to-ring transition (Figure 4J). Second, we found that as rings formed, the fraction of bivalent crosslinkers bound to two filaments increased (Figure 4K). We note that our modeling approaches have some limitations because we model the condensate as a spherical container with rigid boundaries. However, as we showed previously,[18] this assumption does not impact our conclusions about the assembly of shell and ring morphologies, as these structures form during the

(E) Phalloidin-iFluor-594 (red) staining of mini-Lpd condensates (green) with 5 μM monomeric G-actin (unlabeled) added, displaying rings and rods of filamentous actin within the protein condensates. Scale bars, 5 μm.
(F) Representative confocal cross-section images of the progression of condensate deformation as a result of actin filament assembly. Scale bar, 1 μm.
(G) Representative 2D confocal images of independent mini-Lpd condensates (green) containing peripheral actin, shown with phalloidin staining (red), in a shell of actin (top) and a ring of actin (bottom). Scale bars, 1 μm.
(H) 3D reconstructions of the same mini-Lpd condensates shown in (G) demonstrating a shell of actin (top) and a ring of actin (bottom). Scale bars, 1 μm.
(I) Simulations show that bivalent crosslinker kinetics affect actin network organization within condensates. Representative final snapshots (t = 600 s) from simulations at various binding and unbinding rates within spherical condensates (R = 1 μm) containing 30 actin filaments (red) and 1,000 bivalent crosslinkers (green spheres). Please refer to the Methods S1 section for a detailed description of the model. The binding rates of the bivalent crosslinkers are varied along each column, and unbinding rates are varied along each row. See also Video S1. For additional kinetic conditions, see Figure S6E and Video S2.
(J) Dynamics of the actin-covered surface area fraction for varied bivalent crosslinker binding and unbinding kinetics. Data used: 10 replicates.
(K) Stacked bar graphs representing the fraction of bivalent crosslinkers bound to 0, 1, or 2 actin filaments for each condition. The error bars represent the standard deviation. For (J) and (K), 10 replicates are considered per condition, and the data were obtained from the last 30 snapshots (5%) of each replicate. For analysis of additional kinetic conditions, see Figures S6F and S6G.

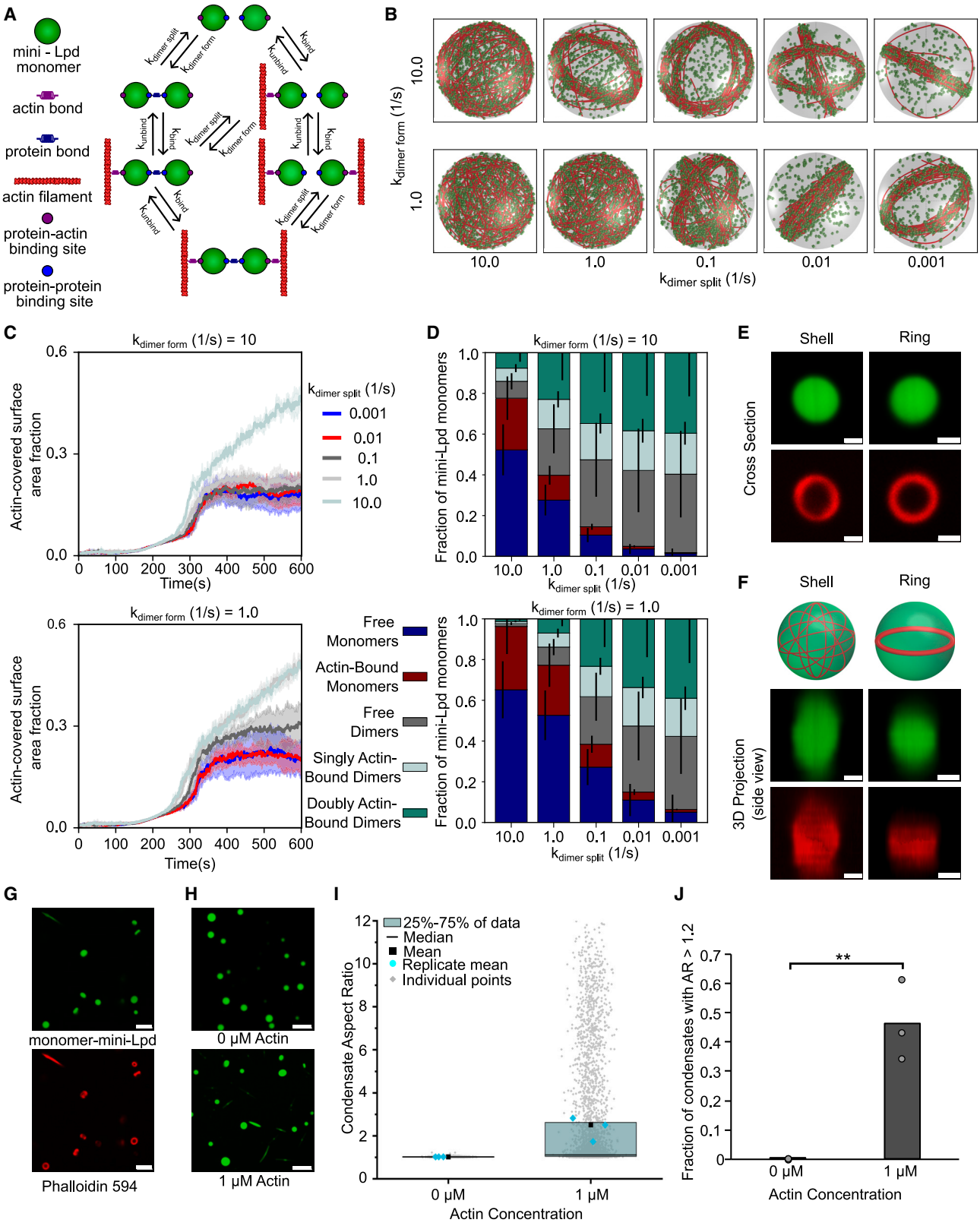

Figure 5. Dynamic protein dimers bundle actin filaments

(A) Schematic showing the different possible binding interactions between the monomeric actin-binding protein and actin, including both protein-protein interactions (dynamic dimerization) and protein-actin interactions.

(legend continued on next page)

period when the condensate is still approximately spherical. While the specific mechanical properties of the condensates used in these experiments are unknown, it is known that the viscosity of biomolecular condensates can range from 10^{-1} to 10^{3} Pa•s.[51] To probe the effect of the viscosity parameter on our model, we simulated the LLPS condensate system with a wide range of viscosities using ring-forming kinetics for VASP-actin binding and found that the viscosity impacted the timescale of ring formation, but not the final ring architecture (Figures S5A and S5B). Additionally, as our simulations model the condensate environment using a fixed volume fraction of crosslinkers, we also compared simulations with an increasing number of crosslinkers, ranging from 1,000 to 20,000, corresponding to crosslinker volume fractions of 2.7%–54%. We found that variation over this range does not alter the final actin architectures (Figures S5C–S5E). This result is consistent with previous findings[18] where it was established that actin network shapes were the result of kinetic trapping and were not sensitive to changes in the copy number of crosslinkers in the simulation.

These results collectively suggest that within the condensate environment, where the concentration of proteins is high, a dimeric actin binder can sufficiently crosslink actin filaments to facilitate the formation of ring-like bundles, which, in experiments, eventually deform and elongate condensates to form linear actin bundles. Further, to mimic condensates consisting of VASP and Lamellipodin (Figure 3), we simulated mixtures of tetravalent and bivalent crosslinkers, which also resulted in a shell-to-ring transition, as expected (Figure S6A; see also Video S3). Our simulations reveal that the ratio of tetravalent to bivalent crosslinkers can tune the balance between shells and rings (Figures S6B–S6D).

Dynamic dimerization of crosslinkers is sufficient to bundle actin filaments within condensates

Having observed in both experiments and simulations that mini-Lpd is sufficient to facilitate actin ring formation and bundling, we wondered to what extent these behaviors depend on the dimeric nature of mini-Lpd. Protein condensates are known to promote multivalent interactions among proteins,[38,52,53] yet stable multimerization of the constituent proteins is not required for condensate formation. On the contrary, some of the best-studied examples of condensate-forming proteins are monomeric under dilute conditions.[10,54] Therefore, we asked whether the inherent multivalency of the condensate environment might be sufficient to facilitate actin bundling. To investigate this question, we simulated monomeric actin-binding proteins that have an affinity for one another and for actin, such that they form dynamically reversible dimers, as may occur when they bind to closely spaced actin filaments (Figure 5A). In this way, monomers can form dimers stochastically by associating and dissociating throughout the simulation, representing transient interactions between monomeric actin-binding proteins inside protein condensates. This dynamic dimerization model has two sets of binding affinities—one for actin binding and another for dimerization (Figure 5A). We investigated the role of dimerization in a regime where actin is already known to form rings when crosslinked by stable dimers (Figures 4I–4K, k_{bind} = 10.0 s^{-1}, k_{unbind} = 1.0 s^{-1}). Our simulations reveal that even when monomers dimerize transiently, actin filaments can still form bundles, given a sufficiently long dimer residence time. In the case of dynamic dimerization, the formation of rings depends on the balance between the association and dissociation of monomers to form dimers (Figure 5B). Notably, this model lacks the necessary biochemical detail to support the calculation of meaningful binding constants for dimerization. When the rate of association is higher than dissociation, the fraction of the condensate inner surface area covered by actin is low, corresponding to a ring state (Figure 5C top). By contrast, when the dissociation rate is higher than the association rate, we observe shells (Figure 5C bottom). Thus, ring formation is favored when dimers have a higher residence time. This result is similar to what has been suggested recently in the literature for diverse actin-interacting

(B) Simulations show that monovalent actin binding can lead to the formation of ring structures when monomers are allowed to interact, bind to form dimers, and function as transient bivalent crosslinkers. Representative final snapshots (t = 600 s) from simulations at various dimer formation and splitting rates within spherical condensates (R = 1 μm) containing 30 actin filaments (red) and 2,000 monomers (green spheres), which can form a maximum of 1,000 dimers. Please refer to the Methods S1 section for a detailed description of the model. The dimer formation rates of the monomers are varied along each column, and dimer splitting rates are varied along each row. Actin-binding kinetics were chosen from previous simulations (Figure 4I) to correspond to ring-forming conditions for bivalent crosslinkers. Also see Video S4.

(C) Time series showing the mean (solid line) and standard deviation (shaded area) of simulated condensate surface that is covered with actin. The $k_{dimer\ form}$ value is shown on top of each subpanel while time series are colored by $k_{dimer\ split}$ values. Data used: 5 replicates. Please refer to the Methods S1 section for a detailed description.

(D) Stacked bar graph showing the distribution of condensate protein at different states, namely, free monomers, free dimers, actin-bound monomers, singly actin-bound dimers, and doubly actin-bound dimers. Error bars show standard deviation. Data used: 5 replicates, data from the last 30 snapshots. A cartoon depiction of each formation can be seen in Figure S6J.

(E) Representative 2D confocal cross sections of independent monomer mini-Lpd (green) condensates containing peripheral actin, shown with phalloidin staining (red), in both a shell of actin (left) and a ring of actin (right). Scale bars, 1 μm.

(F) 3D reconstructions of the same condensates shown in (E), demonstrating a shell of actin (left) and a ring of actin (right). Scale bars, 1 μm.

(G) Phalloidin-iFluor-594 (red) staining of monomer-mini-Lpd condensates (green) with 5 μM monomeric G-actin (unlabeled) added, displaying actin filaments within the protein condensates. Scale bars, 5 μm.

(H) The addition of actin to monomer-mini-Lpd also results in the deformation of protein condensates formed from 5 μM monomer-mini-Lpd. Scale bars, 5 μm.

(I) Distribution of condensate aspect ratios across the conditions in (H), with at least 1,000 condensates analyzed for each condition. For the 1 μM actin condition, values for aspect ratios above 10, corresponding to 2.97% of the data, are not displayed to better visualize distributions for all conditions.

(J) Quantification of the fraction of high-aspect-ratio protein condensates, defined as condensates with aspect ratios >1.2, across the conditions in (H). Data are mean across three independent experiments with at least 1,000 condensates analyzed per condition. Overlaid gray circles denote the means of each replicate. Two asterisks denote $p < 0.01$ using an unpaired, two-tailed t test on the means of the replicates $n = 3$. All experiments were performed in a buffer containing 20 mM Tris (pH 7.4), 50 mM NaCl, 5 mM TCEP, and 3% (w/v) PEG 8000.

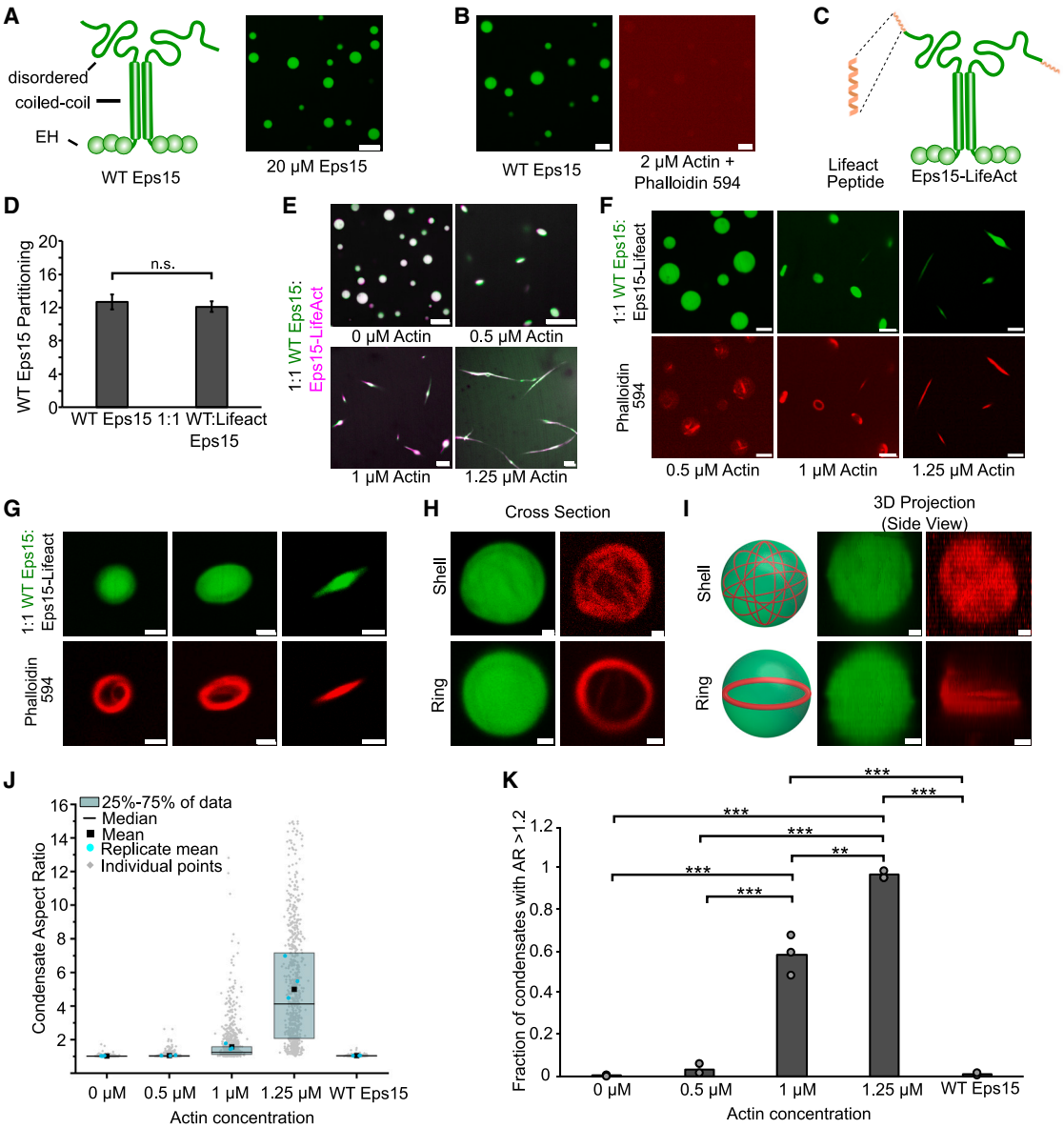

Figure 6. Adding an actin-binding domain to an arbitrary condensate-forming protein is sufficient to confer the ability to assemble and bundle actin filaments

(A) Left: schematic depicting wild-type Eps15 and its major domains. Right: 20 μM wild-type Eps15 forms condensates in solution with 3% (w/v) PEG. Scale bar, 5 μm.

(B) Wild-type Eps15 (green) condensates do not assemble or bundle actin filaments as indicated by the lack of condensate deformation and a lack of phalloidin-stained filaments. Scale bars, 5 μm.

(C) Schematic depicting addition of Lifeact to the C terminus of Eps15.

(D) Partitioning of wild-type Eps15 into condensates formed from only wild-type Eps15 (self-partitioning) and condensates formed with 1:1 wild-type Eps15:Eps15-Lifeact. Data are mean ± standard deviation across three independent experiments.

(E) Representative images of condensate deformation and actin assembly upon the addition of increasing concentrations of monomeric actin to condensates formed of 1:1 WT Eps15:Eps15-Lifeact. Scale bars, 5 μm.

(F) Representative images of phalloidin staining of condensates consisting of 1:1 WT Eps15:Eps15-Lifeact following actin addition. Scale bars, 5 μm.

(G) Representative confocal cross-section images of the progressive, actin-driven deformation of condensates consisting of 1:1 WT Eps15:Eps15-Lifeact. Scale bars, 2 μm.

(H) Representative 2D confocal images of independent 1:1 WT Eps15:Eps15-Lifeact condensates (green) containing peripheral actin, shown with phalloidin staining (red), in both a shell of actin (top) and a ring of actin (bottom). Scale bars, 1 μm.

(I) 3D reconstructions of the same condensates shown in (H), demonstrating a shell of actin (top) and a ring of actin (bottom). Scale bars, 1 μm.

(J) Distribution of condensate aspect ratios across the conditions in (E), with at least 700 condensates analyzed for each condition. For the 1.25 μM actin condition, values for aspect ratios higher than 15, corresponding to 3.5% of the data, are not displayed to better visualize distributions for all conditions.

(legend continued on next page)

proteins, including the Arp2/3 complex and Sos1, where protein condensates facilitate increased actin assembly due to longer residence times of nucleation-promoting factors.[55,56] We next examined the distribution of monomers and dimers bound to actin in these simulations. The actin-binding protein can exist in five subpopulations: free monomers, free dimers, actin-bound monomers, singly actin-bound dimers, and doubly actin-bound dimers. We found that in cases where actin shells predominated, the fraction of monomers bound to actin was higher, while the fraction of dimers bound to actin was negligible. By contrast, conditions that supported the assembly of ring-like actin bundles had a higher fraction of actin-bound dimers (Figure 5D). Here, we chose a propensity for dimer formation as the simplest representation of protein clustering in the condensate environment. The resulting trend of increasing ring formation with increasing dimer affinity would be expected to increase if higher-order multimerization, as is likely present in the condensate environment, were included in the simulations. To investigate this possibility, we simulated monomeric actin-binding proteins as spheres that can dynamically bind up to two other actin-binding proteins and one F-actin molecule, which allows for the formation of higher multimeric states. We found that dynamic multimers of actin-binding proteins still promote actin bundling and ring formation and that the presence of actin promotes the multimerization of actin-binding proteins (Figure S7).

To test the prediction that a stable multimer is not required for actin bundling in protein condensates, we examined a monomeric version of mini-Lpd, which we will refer to as monomer-mini-Lpd. This protein was made monomeric by omitting the dimerizing leucine zipper domain included in the mini-Lpd model protein. Monomer mini-Lpd formed condensates of a similar partition coefficient to those formed from mini-Lpd across varying buffer ionic strengths (Figures S1C and S1D), suggesting that there is little difference in the propensity of the two proteins to form condensates. In line with the model predictions, condensates formed from monomer-mini-Lpd behaved similarly to those of the dimeric mini-Lpd upon exposure to actin. Upon the addition of monomeric actin, actin filaments began to assemble inside the condensates and partitioned to the inner condensate surface, where they were assembled into shells and ring-like bundles (Figures 5E and 5F). We note that there appears to be a slight enrichment of monomer mini-Lpd signal in the center of the condensate when actin is in the ring configuration. This enrichment could result from local enrichment of mini-Lpd by the actin ring. As actin filaments continued to assemble inside the condensates, confirmed through phalloidin staining (Figure 5G), the condensates progressively deformed (Figure 5H), had high aspect ratios (Figures 5I and 5J), and retained liquid-like properties (Figures S3E and S3F) similar to those formed upon the addition of actin to condensates of VASP,[13] VASP/mini-Lpd (Figure 3A), and mini-Lpd (Figure 4A). These results support the findings of the dynamic dimerization (Figure 5) and multimerization (Figure S7) models, showing that transient interactions between monomeric actin-binding proteins are sufficient to facilitate filament bundling in the condensate environment. The ability of condensates composed of proteins that lack any known polymerase activity, mini-Lpd and monomer-mini-Lpd, to assemble and bundle actin filaments led us to ask how protein condensates might facilitate the assembly of actin filaments. Multivalent binding to actin filaments is thought to be a key functional requirement for the two major classes of known polymerases, formins, and members of the ENA/VASP family.[7,15,49] Formins are native dimers, while ENA/VASP proteins are native tetramers.[7,14] Both polymerases function by binding simultaneously to actin filaments and monomeric actin, resulting in the addition of monomers to the barbed ends of growing filaments. Given the essential role of multivalent binding in actin assembly, we wondered whether protein condensates, which strongly promote multivalent protein contacts,[8,9,38] might have an inherent capacity to promote the assembly of actin filaments.

Adding an actin-binding domain to a condensate-forming protein confers the ability to assemble and bundle actin filaments

Next, we sought to identify the minimum requirements for the assembly and bundling of actin filaments by protein condensates. Specifically, we asked whether the binding of multiple condensate proteins to a growing actin filament could function similarly to the binding of filaments by multimeric actin polymerases, effectively meeting the key requirement for actin assembly. To investigate this possibility, we examined the interaction of actin with a condensate-forming protein that has no known ability to bind or facilitate actin assembly and then conferred actin-binding ability upon it through the addition of an actin-binding domain. The protein we selected for this experiment was Eps15, a protein involved in clathrin-mediated endocytosis, which has no known interaction with actin.[57–59] Eps15 has an N-terminal region consisting of three structured Eps15-homology (EH) domains, a central coiled-coil domain, through which the protein forms native dimers, and an intrinsically disordered C-terminal domain.[36] Binding interactions between the N- and C-terminal domains drive Eps15 to form protein condensates *in vitro* (Figure 6A).[34] As expected, the addition of 2 μM monomeric actin to Eps15 condensates did not result in actin filament assembly, as no filaments were observed upon phalloidin staining, and the condensates did not deform (Figure 6B). We then fused a filamentous actin-binding motif, the 17 amino acid Lifeact peptide, to the C terminus of Eps15 to create Eps15-Lifeact (Figure 6C). Lifeact, which binds to actin filaments at the interface between two monomers, is commonly used in conjunction with fluorophores to visualize the filamentous actin cytoskeleton.[60–62] It does not alter the bulk assembly rate of growing actin filaments,[60] though it can increase the initial rate of barbed end elongation, likely by stabilizing nascent filaments.[63] Mixing WT Eps15 and Eps15-Lifeact at a 1:1 ratio (15 μM total protein) in the presence of 3% PEG (w/v) led to the co-condensation of the two proteins. Condensates were

(K) Quantification of the fraction of elongated protein condensates, defined as condensates with aspect ratios >1.2, across the conditions in (E). Data are mean ± standard deviation across three independent experiments with at least 700 condensates analyzed in total per condition. Overlaid gray circles denote the means of each replicate. Two asterisks denote $p < 0.01$, and three asterisks denote $p < 0.001$ using an unpaired, two-tailed t test on the means of the replicates $n = 3$. All experiments were performed in a buffer containing 20 mM Tris (pH 7.4), 150 mM NaCl, 5 mM TCEP, and 3% (w/v) PEG 8000.

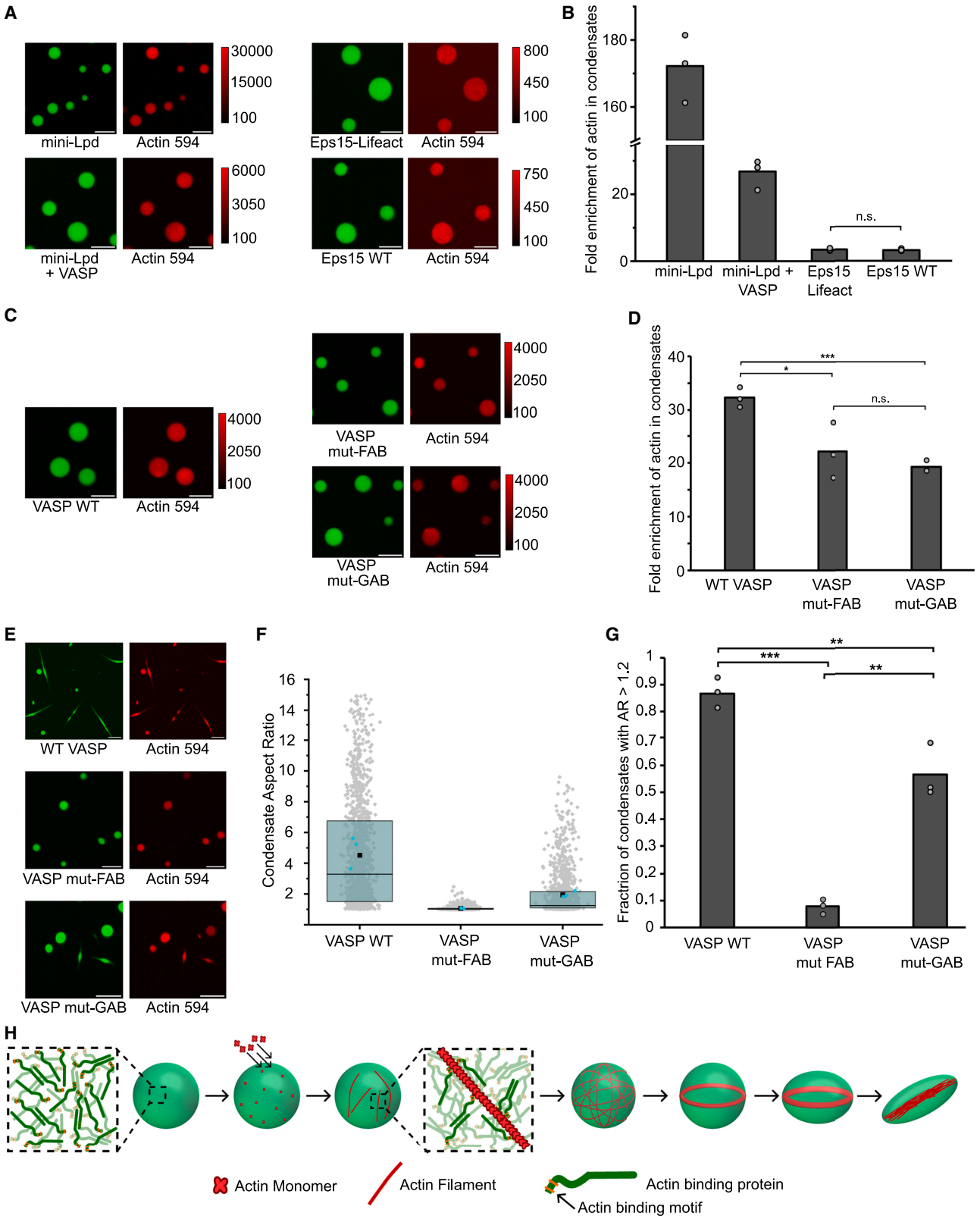

Figure 7. Actin enrichment analysis suggests a need for F-actin binding by condensate proteins for actin assembly

(A) Representative images using 500 nM Atto 594-labeled G-actin to measure actin partitioning into condensates formed from 5 μM mini-Lpd, 5 μM mini-Lpd + 10 μM VASP, 15 μM of a 1:1 ratio of WT Eps15 and Eps15-Lifeact, or 15 μM WT Eps15. Buffer conditions were 20 mM Tris pH 7.4, either 50 mM NaCl for mini-Lpd

(legend continued on next page)

formed using this 1:1 ratio to minimize any potential effect of Lifeact on Eps15 phase separation. The partitioning of WT Eps15 into these condensates was similar to that of condensates consisting purely of WT Eps15, suggesting that addition of Lifeact had little effect on Eps15 phase separation (Figure 6D). When monomeric actin was added to the resulting condensates, they deformed into high-aspect-ratio structures (Figure 6E) and retained liquid-like properties after deformation by actin filament assembly (Figures S3G, S3H, and S3K). Actin assembly within these condensates was confirmed by phalloidin staining, which revealed the progressive deformation of condensates from spherical to ellipsoid to rod-like morphologies (Figures 6F and 6G). Prior to these morphological transitions, actin shells and ring-like bundles formed within spherical condensates (Figures 6H and 6I), as described above for condensates of mini-Lpd (Figures 4G and 4H) and monomer-mini-Lpd (Figures 5E and 5F), and previously for condensates of VASP.[13] Quantification of condensate morphologies confirmed that increasing concentrations of monomeric actin drove a substantial increase in the aspect ratios of condensates (Figures 6J and 6K).

F-actin binding by condensate-forming proteins is crucial for actin filament assembly

What are the key requirements for the assembly and bundling of actin filaments by protein condensates? Is it simply a matter of locally concentrating G-actin? Or is it necessary to present filamentous actin-binding domains that might stabilize nascent filament nuclei? To address these questions, we sought to determine whether the ability of condensates to assemble actin filaments correlated with the ability to concentrate G-actin, the presence of F-actin-binding motifs, or both. To probe the ability of condensates to locally concentrate G-actin, we added 500 nM fluorescently labeled G-actin to preformed condensates. Latrunculin A (5 μM) was included in these experiments to prevent actin assembly. G-actin partitioned strongly into condensates formed from mini-Lpd + VASP and mini-Lpd alone, showing greater than 25-fold enrichment relative to the surrounding solution for mini-Lpd and VASP and greater than 150-fold enrichment for condensates composed of mini-Lpd alone (Figures 7A and 7B). Notably, the high degree of enrichment in mini-Lpd condensates is likely due to their formation in a buffer containing 50 mM NaCl, as actin-binding proteins are known to bind actin more strongly as ionic strength decreases.[64] Surprisingly, Eps15-Lifeact-containing condensates only weakly concentrated actin, and to the same degree as WT Eps15 condensates, with actin being enriched about 3-fold compared with the surrounding solution (Figures 7A and 7B). This weak concentration of actin monomers is in the range for nonspecific recruitment of protein to phase-separated condensates,[65] suggesting that the addition of Lifeact does not contribute significantly to G-actin binding. Notably, while fluorescein-Lifeact has been shown to bind G-actin, when Lifeact is attached to a bulkier domain, it loses its ability to bind G-actin,[60,63] likely explaining the inability of Eps15-Lifeact condensates to concentrate G-actin. As shown in the previous section, Eps15-Lifeact condensates assembled and bundled actin filaments (Figure 6E), while WT Eps15 condensates failed to do so even at high actin concentrations (Figure 6B) Taken together, these data suggest that the ability to concentrate G-actin is not well correlated with condensate-mediated actin assembly. Next, we probed the impact of F-actin-binding motifs on condensate-mediated actin assembly and bundling. Here, we investigated the impact of VASP's actin-interacting domains on the ability of VASP condensates to facilitate actin assembly. We first examined G-actin partitioning into condensates formed from WT VASP and VASP mutants lacking functional F-actin (VASP mut-FAB [FAB, F-actin-binding site]) or G-actin (VASP mut-GAB [GAB, G-actin-binding site]) binding domains. We found that G-actin partitions almost equally (about 20-fold enrichment; Figures 7C and 7D) into condensates composed of these mutants but to a lesser degree in comparison with condensates composed of WT VASP, suggesting that both GAB and FAB impact actin recruitment to VASP condensates. Surprisingly, condensates of VASP mut-GAB were still able to facilitate the assembly and bundling of actin filaments, which led to condensate deformation, albeit to a lesser extent than full-length VASP. By contrast, condensates of VASP mut-FAB almost completely lacked the ability to assemble and bundle actin filaments, showing almost no deformation upon actin addition (Figures 7E–7G). The inability of VASP mut-FAB condensates to assemble actin, despite a strong ability to concentrate G-actin, further confirms that concentrating G-actin is insufficient for condensate-mediated assembly of actin filaments. Collectively, these findings illustrate that filamentous actin binding is the key requirement for condensate-mediated actin assembly.

DISCUSSION

Taken together, our findings suggest that multivalent interactions with filamentous actin are sufficient for the assembly and bundling of actin filaments by protein condensates (Figure 7H). Specifically, when condensates are exposed to actin, the

or 150 mM NaCl (for all other proteins), 5 mM TCEP, with 5 μM latrunculin A included to avoid any contribution from actin assembly. 3% w/v PEG 8000 was included for the condensate formation of all protein combinations except mini-Lpd + VASP, consistent with experiments in the main text. All scale bars, 5 μm.
(B) Quantification of actin partitioning into condensates shown in (A).
(C) Representative images using 500 nM Atto 594-labeled G-actin to measure actin partitioning into condensates formed from 20 μM VASP WT, 20 μM VASP mut-FAB, or 20 μM VASP mut-GAB. Buffer conditions were 20 mM Tris pH 7.4, 150 mM NaCl, 5 mM TCEP, 5 μM latrunculin A, and 3% w/v PEG. All scale bars, 5 μm.
(D) Quantification of actin partitioning into condensates formed from the proteins in (C).
(E) Condensates formed from 15 μM VASP or associated VASP mutants upon adding 2 μM G-actin. All scale bars, 5 μm.
(F) Distribution of condensate aspect ratios across the conditions in (E), with at least 800 condensates analyzed for each condition.
(G) Quantification of the fraction of high-aspect-ratio protein condensates, defined as condensates with aspect ratios >1.2, across the conditions in (E).
(H) Cartoon depicting the proposed mechanism of actin assembly and bundling by condensates of actin-binding proteins.
All bar graphs represent the average across three independent experiments. The overlaid gray circles denote the averages for each replicate. One asterisk denotes $p < 0.05$, two asterisks denote $p < 0.01$, and three asterisks denote $p < 0.001$ using an unpaired, two-tailed t test on the means of the replicates $N = 3$. All scale bars, 5 μm.

assembly of actin filaments results from multivalent interactions between filament nuclei and filamentous actin-binding motifs. As actin filaments grow within condensates, they spontaneously partition to the edges of condensates to minimize filament curvature energy. This phenomenon has been reported whenever filaments grow inside spherical containers with diameters below the persistence length of actin, 10–20 μm.[13,18,66–68] This partitioning results in the assembly of actin shells at the inner surfaces of the condensate, which rearrange to form ring-like actin bundles. As more filaments join these structures, their rigidity eventually overcomes the surface tension of the condensate, permitting the filaments to straighten and thereby deforming the condensate into a rod-like structure filled with a bundle of parallel actin filaments.[13] Here, we have used a combination of *in vitro* experiments and agent-based computational modeling to illustrate that transient interactions between condensate-forming proteins are sufficient to facilitate this process.

Notably, our studies did not reveal the precise mechanism of filament nucleation, a key early step in filament assembly. In cells, nucleation-promotion factors are used to initiate actin filament assembly. The best studied of these are Arp2/3 and formin, which are responsible for much of the nucleation of actin filaments in the cell.[7,69–71] However, proteins that bind multiple actin monomers in tandem, such as Spire, Cobl, and JMY, also nucleate actin filaments independent of Arp2/3 or formin.[32,72–77] We speculate that nascent filaments within the condensate environment are stabilized in a similar manner through multivalent contacts with condensate-forming proteins that contain filamentous actin-binding sites. Filament assembly by condensates of actin-binding proteins could also provide the initial filaments required for daughter filament nucleation by Arp2/3, fulfilling a similar role to that suggested for filament nucleation by tandem monomer-binding proteins like JMY.[73] We also demonstrate that condensates of actin-binding proteins facilitate filament elongation in the absence of canonical actin polymerases such as formins or ENA/VASP proteins. This finding is reminiscent of what has been shown in recent work, where surface-associated WASP family proteins promote the elongation of nearby actin filaments in a system lacking Arp2/3.[78] Recent work has also shown that monomeric ENA/VASP proteins, which lack polymerase activity, facilitate elongation of actin filaments when concentrated on surfaces.[79,80] These findings, along with our work, suggest that actin-binding proteins may function as actin polymerases when concentrated or clustered together, as is the case in the condensate environment.

However, other potential mechanisms could play a role in filament assembly and bundling within protein condensates. While we did not observe long, non-diffraction-limited filaments forming in solution (Figure S2), small, diffraction-limited filaments could be forming there and then joining the condensates. Annealing of short filaments is a favorable reaction, and recent studies show that crowded hydrophilic surfaces can enhance the annealing rate.[81,82] Phase-separated condensates, which present crowded environments, might similarly promote the annealing of nascent filaments that either partition into or form within the condensate. There could also be contributions to both filament assembly and bundling from depletion interactions or bridging of actin filaments by filament-bound proteins. Depletion interactions have been shown to contribute to filament bundling and likely assist in condensate-mediated filament bundling.[68,83,84] Filament wetting by the liquid-like protein phase also likely contributes to filament bundling. Our data do not explicitly distinguish between these potential mechanisms and the mechanism proposed in Figure 7F. Elucidating the precise mechanisms by which protein condensates contribute to filament nucleation and elongation is an important area of future work. Many actin-interacting proteins contain both proline-rich sequences and proline-binding domains, such as Src homology 3 (SH3), EVH1, or WW domains.[14,38,85,86] Interactions between these domains and sequences often lead to the assembly of multivalent protein networks, which are the building blocks of liquid-like condensates.[11,38,87] In line with this reasoning, recent work in several labs has shown that many actin-interacting proteins participate in condensate networks or form condensates themselves and that many of these condensates facilitate actin assembly.[11,13,23,37–41] For example, our previous work showed that VASP condensates incorporate Arp2/3 and thereby facilitate the formation of branched actin networks.[23] In addition to providing a platform for the assembly of actin-binding proteins, condensates also increase the dwell time of nucleation-promotion factors, thereby increasing the activity of Arp2/3 and promoting actin assembly.[11,56] Thus, the ability of actin-binding condensates to nucleate and facilitate actin assembly likely works synergistically with canonical nucleators and polymerases such as Arp2/3, formins, and ENA/VASP proteins. In this context, specialized nucleators or polymerases may enhance the control of actin network morphology or boost elongation and nucleation rates within condensates. An important goal for future work is to understand how phase separation of actin-binding proteins synergizes with canonical actin polymerases to regulate actin assembly. By illustrating that the assembly and bundling of actin filaments can occur in the absence of proteins with inherent polymerase or nucleation activity, our findings suggest that the set of proteins involved in cytoskeletal assembly may be substantially larger than previously thought. Actin has a large interactome consisting of more than 100 proteins,[87] only a small fraction of which are known to facilitate the assembly of actin filaments. Our studies suggest that the condensate environment has an inherent capacity to promote flexible, multivalent contacts between actin filaments and condensate proteins.

Limitations of the study

The most significant limitation of this study is that proposed mechanisms are yet to be evaluated in the context of living cells and organisms. A further limitation is that, while our work reveals the role of protein condensates in the assembly and bundling of actin filaments, the precise mechanism of filament assembly, specifically filament nucleation and elongation, has not been revealed.

RESOURCE AVAILABILITY

Lead contact

Further information and requests for resources and reagents should be directed to and will be fulfilled by the lead contact, Jeanne Stachowiak (jcstach@austin.utexas.edu).

Materials availability

All unique/stable reagents generated in this study are available from the lead contact with a completed material transfer agreement.

Data and code availability

Microscopy data and analysis will be shared by the lead contact upon request. The Cytosim input files and data files are available on GitHub (https://github.com/RangamaniLabUCSD/Dynamic_multimerization) and at https://doi.org/10.5281/zenodo.14522973. The custom Cytosim code used to generate trajectories and the Python scripts used to analyze trajectories are available on GitHub (https://github.com/RangamaniLabUCSD/Dynamic_multimerization) and at https://doi.org/10.5281/zenodo.14522973. Any additional information required to reanalyze the data reported in this work paper is available from the lead contact upon request.

STAR★METHODS

Detailed methods are provided in the online version of this paper and include the following:

- KEY RESOURCES TABLE
- EXPERIMENTAL MODEL AND STUDY PARTICIPANT DETAILS
- METHOD DETAILS
  - Plasmids
  - Protein Purification
  - Protein labeling
  - Protein condensate formation and actin filament assembly
  - Microscopy
  - Image Analysis
  - Modeling
- QUANTIFICATION AND STATISTICAL ANALYSIS

ACKNOWLEDGMENTS

This research was supported by the National Science Foundation through the Center for Dynamics and Control of Materials: an NSF MRSEC under cooperative agreement no. DMR-2308817. Additionally, this research was supported by grants from the NIH to J.C.S. (R35GM139531) and P.R. (R01GM132106) and by the NSF through a Modulus grant MCB 2327244 to P.R and J.C.S.

AUTHOR CONTRIBUTIONS

C.W., K.G., A.C., D.M., P.R., and J.C.S. designed experiments. C.W., K.G., A.C., D.M., P.R., and J.C.S. wrote and edited the manuscript. C.W., K.G., A.C., D.M., A.T., L.W., E.M.L., P.R., and J.C.S. performed experiments and analyzed data. All authors consulted on manuscript preparation and editing.

DECLARATION OF INTERESTS

The authors declare no competing interests.

SUPPLEMENTAL INFORMATION

Supplemental information can be found online at https://doi.org/10.1016/j.devcel.2025.01.012.

Received: May 21, 2024
Revised: October 30, 2024
Accepted: January 15, 2025
Published: February 5, 2025

REFERENCES

1. Fletcher, D.A., and Mullins, R.D. (2010). Cell mechanics and the cytoskeleton. Nature *463*, 485–492. https://doi.org/10.1038/nature08908.
2. Hinze, C., and Boucrot, E. (2018). Local actin polymerization during endocytic carrier formation. Biochem. Soc. Trans. *46*, 565–576. https://doi.org/10.1042/BST20170355.
3. Pollard, T.D., and Cooper, J.A. (2009). Actin, a central player in cell shape and movement. Science *326*, 1208–1212. https://doi.org/10.1126/science.1175862.
4. Vasioukhin, V., Bauer, C., Yin, M., and Fuchs, E. (2000). Directed actin polymerization is the driving force for epithelial cell–cell adhesion. Cell *100*, 209–219. https://doi.org/10.1016/S0092-8674(00)81559-7.
5. Campellone, K.G., and Welch, M.D. (2010). A nucleator arms race: cellular control of actin assembly. Nat. Rev. Mol. Cell Biol. *11*, 237–251. https://doi.org/10.1038/nrm2867.
6. Dominguez, R. (2009). Actin filament nucleation and elongation factors – structure–function relationships. Crit. Rev. Biochem. Mol. Biol. *44*, 351–366. https://doi.org/10.3109/10409230903277340.
7. Chesarone, M.A., DuPage, A.G., and Goode, B.L. (2010). Unleashing formins to remodel the actin and microtubule cytoskeletons. Nat. Rev. Mol. Cell Biol. *11*, 62–74. https://doi.org/10.1038/nrm2816.
8. Alberti, S., Gladfelter, A., and Mittag, T. (2019). Considerations and challenges in studying liquid-liquid phase separation and biomolecular condensates. Cell *176*, 419–434. https://doi.org/10.1016/j.cell.2018.12.035.
9. Boeynaems, S., Alberti, S., Fawzi, N.L., Mittag, T., Polymenidou, M., Rousseau, F., Schymkowitz, J., Shorter, J., Wolozin, B., Van Den Bosch, L., et al. (2018). Protein phase separation: A new phase in cell Biology. Trends Cell Biol. *28*, 420–435. https://doi.org/10.1016/j.tcb.2018.02.004.
10. Elbaum-Garfinkle, S., Kim, Y., Szczepaniak, K., Chen, C.C.-H., Eckmann, C.R., Myong, S., and Brangwynne, C.P. The disordered P granule protein LAF-1 drives phase separation into droplets with tunable viscosity and dynamics. J. Comput. Biol. 6.
11. Su, X., Ditlev, J.A., Hui, E., Xing, W., Banjade, S., Okrut, J., King, D.S., Taunton, J., Rosen, M.K., and Vale, R.D. (2016). Phase separation of signaling molecules promotes T cell receptor signal transduction. Science *352*, 595–599. https://doi.org/10.1126/science.aad9964.
12. Woodruff, J.B., Ferreira Gomes, B., Widlund, P.O., Mahamid, J., Honigmann, A., and Hyman, A.A. (2017). The centrosome is a selective condensate that nucleates microtubules by concentrating tubulin. Cell *169*, 1066–1077.e10. https://doi.org/10.1016/j.cell.2017.05.028.
13. Graham, K., Chandrasekaran, A., Wang, L., Ladak, A., Lafer, E.M., Rangamani, P., and Stachowiak, J.C. (2023). Liquid-like VASP condensates drive actin polymerization and dynamic bundling. Nat. Phys. *19*, 574–585. https://doi.org/10.1038/s41567-022-01924-1.
14. Krause, M., Dent, E.W., Bear, J.E., Loureiro, J.J., and Gertler, F.B. (2003). Ena/VASP Proteins: regulators of the actin cytoskeleton and cell migration. Annu. Rev. Cell Dev. Biol. *19*, 541–564. https://doi.org/10.1146/annurev.cellbio.19.050103.103356.
15. Hansen, S.D., and Mullins, R.D. (2010). VASP is a processive actin polymerase that requires monomeric actin for barbed end association. J. Cell Biol. *191*, 571–584. https://doi.org/10.1083/jcb.201003014.
16. Kühnel, K., Jarchau, T., Wolf, E., Schlichting, I., Walter, U., Wittinghofer, A., and Strelkov, S.V. (2004). The VASP tetramerization domain is a right-handed coiled coil based on a 15-residue repeat. Proc. Natl. Acad. Sci. USA *101*, 17027–17032. https://doi.org/10.1073/pnas.0403069101.
17. Isambert, H., Venier, P., Maggs, A.C., Fattoum, A., Kassab, R., Pantaloni, D., and Carlier, M.F. (1995). Flexibility of actin filaments derived from thermal fluctuations: EFFECT OF BOUND NUCLEOTIDE, PHALLOIDIN, AND MUSCLE REGULATORY PROTEINS *. J. Biol. Chem. *270*, 11437–11444. https://doi.org/10.1074/jbc.270.19.11437.
18. Chandrasekaran, A., Graham, K., Stachowiak, J.C., and Rangamani, P. (2024). Kinetic trapping organizes actin filaments within liquid-like protein droplets. Nat. Commun. *15*, 3139. https://doi.org/10.1038/s41467-024-46726-6.
19. Lafuente, E.M., Van Puijenbroek, A.A.F.L., Krause, M., Carman, C.V., Freeman, G.J., Berezovskaya, A., Constantine, E., Springer, T.A., Gertler, F.B., and Boussiotis, V.A. (2004). RIAM, an Ena/VASP and profilin ligand, interacts with Rap1-GTP and mediates Rap1-induced adhesion. Dev. Cell *7*, 585–595. https://doi.org/10.1016/j.devcel.2004.07.021.

20. Krause, M., Leslie, J.D., Stewart, M., Lafuente, E.M., Valderrama, F., Jagannathan, R., Strasser, G.A., Rubinson, D.A., Liu, H., Way, M., et al. (2004). Lamellipodin, an Ena/VASP ligand, is implicated in the regulation of lamellipodial dynamics. Dev. Cell *7*, 571–583. https://doi.org/10.1016/j.devcel.2004.07.024.

21. Krause, M., Sechi, A.S., Konradt, M., Monner, D., Gertler, F.B., and Wehland, J. (2000). Fyn-binding protein (Fyb)/Slp-76–Associated protein (slap), Ena/Vasodilator-Stimulated Phosphoprotein (Vasp) proteins and the Arp2/3 complex link T cell receptor (Tcr) signaling to the actin cytoskeleton. J. Cell Biol. *149*, 181–194. https://doi.org/10.1083/jcb.149.1.181.

22. Drees, B., Friederich, E., Fradelizi, J., Louvard, D., Beckerle, M.C., and Golsteyn, R.M. (2000). Characterization of the interaction between zyxin and members of the Ena/vasodilator-stimulated phosphoprotein family of proteins. J. Biol. Chem. *275*, 22503–22511. https://doi.org/10.1074/jbc.M001698200.

23. Graham, K., Chandrasekaran, A., Wang, L., Yang, N., Lafer, E.M., Rangamani, P., and Stachowiak, J.C. (2024). Liquid-like condensates mediate competition between actin branching and bundling. Proc. Natl. Acad. Sci. USA *121*, e2309152121. https://doi.org/10.1073/pnas.2309152121.

24. Cheng, K.W., and Mullins, R.D. (2020). Initiation and disassembly of filopodia tip complexes containing VASP and lamellipodin. Mol. Biol. Cell *31*, 2021–2034. https://doi.org/10.1091/mbc.E20-04-0270.

25. Hansen, S.D., and Mullins, R.D. (2015). Lamellipodin promotes actin assembly by clustering Ena/VASP proteins and tethering them to actin filaments. eLife *4*, e06585. https://doi.org/10.7554/eLife.06585.

26. Montaño-Rendón, F., Walpole, G.F.W., Krause, M., Hammond, G.R.V., Grinstein, S., and Fairn, G.D. (2022). PtdIns$_{(3,4)}$P2, Lamellipodin, and VASP Coordinate Cytoskeletal Remodeling during Phagocytic Cup Formation in Macrophages (Cell Biology). J. Cell Biol. *221*, e202207042. https://doi.org/10.1101/2022.03.08.483476.

27. Dimchev, G., Amiri, B., Humphries, A.C., Schaks, M., Dimchev, V., Stradal, T.E.B., Faix, J., Krause, M., Way, M., Falcke, M., et al. (2020). Lamellipodin tunes cell migration by stabilizing protrusions and promoting adhesion formation. J. Cell Sci. *133*, jcs239020. https://doi.org/10.1242/jcs.239020.

28. Chang, Y.-C., Zhang, H., Brennan, M.L., and Wu, J. (2013). Crystal structure of Lamellipodin implicates diverse functions in actin polymerization and Ras signaling. Protein Cell *4*, 211–219. https://doi.org/10.1007/s13238-013-2082-5.

29. Gorai, S., Paul, D., Haloi, N., Borah, R., Santra, M.K., and Manna, D. (2016). Mechanistic insights into the phosphatidylinositol binding properties of the pleckstrin homology domain of lamellipodin. Mol. Biosyst. *12*, 747–757. https://doi.org/10.1039/C5MB00731C.

30. Pokrant, T., Hein, J.I., Körber, S., Disanza, A., Pich, A., Scita, G., Rottner, K., and Faix, J. (2023). Ena/VASP clustering at microspike tips involves lamellipodin but not I-BAR proteins, and absolutely requires unconventional myosin-X. Proc. Natl. Acad. Sci. USA *120*, e2217437120. https://doi.org/10.1073/pnas.2217437120.

31. Mondal, S., Narayan, K., Botterbusch, S., Powers, I., Zheng, J., James, H.P., Jin, R., and Baumgart, T. (2022). Multivalent interactions between molecular components involved in fast endophilin mediated endocytosis drive protein phase separation. Nat. Commun. *13*, 5017. https://doi.org/10.1038/s41467-022-32529-0.

32. Pollard, T.D. (2016). Actin and actin-binding proteins. Cold Spring Harb. Perspect. Biol. *8*, a018226. https://doi.org/10.1101/cshperspect.a018226.

33. Winkelman, J.D., Bilancia, C.G., Peifer, M., and Kovar, D.R. (2014). Ena/VASP Enabled is a highly processive actin polymerase tailored to self-assemble parallel-bundled F-actin networks with fascin. Proc. Natl. Acad. Sci. USA *111*, 4121–4126. https://doi.org/10.1073/pnas.1322093111.

34. Day, K.J., Kago, G., Wang, L., Richter, J.B., Hayden, C.C., Lafer, E.M., and Stachowiak, J.C. (2021). Liquid-like protein interactions catalyse assembly of endocytic vesicles. Nat. Cell Biol. *23*, 366–376. https://doi.org/10.1038/s41556-021-00646-5.

35. Tebar, F., Sorkina, T., Sorkin, A., Ericsson, M., and Kirchhausen, T. (1996). Eps15 is a component of clathrin-coated pits and vesicles and is located at the rim of coated pits. J. Biol. Chem. *271*, 28727–28730. https://doi.org/10.1074/jbc.271.46.28727.

36. Cupers, P., Haar, E. ter, Boll, W., and Kirchhausen, T. (1997). Parallel dimers and anti-parallel tetramers formed by epidermal growth factor receptor pathway substrate Clone 15. J. Biol. Chem. *272*, 33430–33434. https://doi.org/10.1074/jbc.272.52.33430.

37. Cheng, X., Ullo, M.F., and Case, L.B. (2022). Reconstitution of phase-separated signaling clusters and actin polymerization on supported lipid bilayers. Front. Cell Dev. Biol. *10*, 932483. https://doi.org/10.3389/fcell.2022.932483.

38. Li, P., Banjade, S., Cheng, H.-C., Kim, S., Chen, B., Guo, L., Llaguno, M., Hollingsworth, J.V., King, D.S., Banani, S.F., et al. (2012). Phase transitions in the assembly of multivalent signalling proteins. Nature *483*, 336–340. https://doi.org/10.1038/nature10879.

39. Tsukita, K., Kitamata, M., Kashihara, H., Yano, T., Fujiwara, I., Day, T.F., Katsuno, T., Kim, J., Takenaga, F., Tanaka, H., et al. (2023). Phase separation of an actin nucleator by junctional microtubules regulates epithelial function. Sci. Adv. *9*, eadf6358. https://doi.org/10.1126/sciadv.adf6358.

40. Yang, S., Liu, C., Guo, Y., Li, G., Li, D., Yan, X., and Zhu, X. (2022). Self-construction of actin networks through phase separation–induced abLIM1 condensates. Proc. Natl. Acad. Sci. USA *119*, e2122420119. https://doi.org/10.1073/pnas.2122420119.

41. Yu, Y., and Yoshimura, S.H. (2023). Self-assembly of CIP4 drives actin-mediated asymmetric pit-closing in clathrin-mediated endocytosis. Nat. Commun. *14*, 4602. https://doi.org/10.1038/s41467-023-40390-y.

42. Romero, P., Obradovic, Z., Li, X., Garner, E.C., Brown, C.J., and Dunker, A.K. (2001). Sequence complexity of disordered protein. Proteins *42*, 38–48. https://doi.org/10.1002/1097-0134(20010101)42:1<38::AID-PROT50>3.0.CO;2-3.

43. Sun, J., Qu, J., Zhao, C., Zhang, X., Liu, X., Wang, J., Wei, C., Liu, X., Wang, M., Zeng, P., et al. (2024). Precise prediction of phase-separation key residues by machine learning. Nat. Commun. *15*, 2662. https://doi.org/10.1038/s41467-024-46901-9.

44. Mitrea, D.M., Cika, J.A., Stanley, C.B., Nourse, A., Onuchic, P.L., Banerjee, P.R., Phillips, A.H., Park, C.-G., Deniz, A.A., and Kriwacki, R.W. (2018). Self-interaction of NPM1 modulates multiple mechanisms of liquid–liquid phase separation. Nat. Commun. *9*, 842. https://doi.org/10.1038/s41467-018-03255-3.

45. Molliex, A., Temirov, J., Lee, J., Coughlin, M., Kanagaraj, A.P., Kim, H.J., Mittag, T., and Taylor, J.P. (2015). Phase separation by low complexity domains promotes stress granule assembly and drives pathological fibrillization. Cell *163*, 123–133. https://doi.org/10.1016/j.cell.2015.09.015.

46. Uversky, V.N. (2009). Intrinsically disordered proteins and their environment: effects of strong denaturants, temperature, pH, counter ions, membranes, binding partners, osmolytes, and macromolecular crowding. Protein J. *28*, 305–325. https://doi.org/10.1007/s10930-009-9201-4.

47. Brangwynne, C.P., Tompa, P., and Pappu, R.V. (2015). Polymer physics of intracellular phase transitions. Nat. Phys. *11*, 899–904. https://doi.org/10.1038/nphys3532.

48. Narayan, K.B., Baeyens, L., James, H.P., Swain, A., and Baumgart, T. (2024). Fluorescence imaging of lamellipodin-mediated biomolecular condensates on solid supported lipid bilayer membranes. Methods Enzymol. *700*, 33–48. https://doi.org/10.1016/bs.mie.2024.04.007.

49. Bachmann, C., Fischer, L., Walter, U., and Reinhard, M. (1999). The EVH2 domain of the vasodilator-stimulated phosphoprotein mediates tetramerization, F-actin binding, and actin bundle formation. J. Biol. Chem. *274*, 23549–23557. https://doi.org/10.1074/jbc.274.33.23549.

50. Morton, W.M., Ayscough, K.R., and McLaughlin, P.J. (2000). Latrunculin alters the actin-monomer subunit interface to prevent polymerization. Nat. Cell Biol. *2*, 376–378. https://doi.org/10.1038/35014075.

51. Wang, H., Kelley, F.M., Milovanovic, D., Schuster, B.S., and Shi, Z. (2021). Surface tension and viscosity of protein condensates quantified by

micropipette aspiration. Biophys. Rep. *1*, 100011. https://doi.org/10.1016/j.bpr.2021.100011.

52. Banani, S.F., Lee, H.O., Hyman, A.A., and Rosen, M.K. (2017). Biomolecular condensates: organizers of cellular biochemistry. Nat. Rev. Mol. Cell Biol. *18*, 285–298. https://doi.org/10.1038/nrm.2017.7.
53. Hyman, A.A., Weber, C.A., and Jülicher, F. (2014). Liquid-liquid phase separation in Biology. Annu. Rev. Cell Dev. Biol. *30*, 39–58. https://doi.org/10.1146/annurev-cellbio-100913-013325.
54. Burke, K.A., Janke, A.M., Rhine, C.L., and Fawzi, N.L. (2015). Residue-by-residue view of in vitro FUS granules that bind the C-terminal domain of RNA polymerase II. Mol. Cell *60*, 231–241. https://doi.org/10.1016/j.molcel.2015.09.006.
55. Case, L.B., Zhang, X., Ditlev, J.A., and Rosen, M.K. (2019). Stoichiometry controls activity of phase-separated clusters of actin signaling proteins. Science *363*, 1093–1097. https://doi.org/10.1126/science.aau6313.
56. Huang, W.Y.C., Alvarez, S., Kondo, Y., Lee, Y.K., Chung, J.K., Lam, H.Y.M., Biswas, K.H., Kuriyan, J., and Groves, J.T. (2019). A molecular assembly phase transition and kinetic proofreading modulate Ras activation by SOS. Science *363*, 1098–1103. https://doi.org/10.1126/science.aau5721.
57. Benmerah, A., Lamaze, C., Bègue, B., Schmid, S.L., Dautry-Varsat, A., and Cerf-Bensussan, N. (1998). AP-2/Eps15 interaction is required for receptor-mediated endocytosis. J. Cell Biol. *140*, 1055–1062. https://doi.org/10.1083/jcb.140.5.1055.
58. Fazioli, F., Minichiello, L., Matoškovā, B., Wong, W.T., and Di Fiore, P.P. (1993). eps15, A novel tyrosine kinase substrate, exhibits transforming activity. Mol. Cell. Biol. *13*, 5814–5828. https://doi.org/10.1128/mcb.13.9.5814-5828.1993.
59. Henne, W.M., Boucrot, E., Meinecke, M., Evergren, E., Vallis, Y., Mittal, R., and McMahon, H.T. (2010). FCHo proteins are nucleators of clathrin-mediated endocytosis. Science *328*, 1281–1284. https://doi.org/10.1126/science.1188462.
60. Riedl, J., Crevenna, A.H., Kessenbrock, K., Yu, J.H., Neukirchen, D., Bista, M., Bradke, F., Jenne, D., Holak, T.A., Werb, Z., et al. (2008). Lifeact: a versatile marker to visualize F-actin. Nat. Methods *5*, 605–607. https://doi.org/10.1038/nmeth.1220.
61. Schachtner, H., Li, A., Stevenson, D., Calaminus, S.D.J., Thomas, S.G., Watson, S.P., Sixt, M., Wedlich-Soldner, R., Strathdee, D., and Machesky, L.M. (2012). Tissue inducible Lifeact expression allows visualization of actin dynamics in vivo and ex vivo. Eur. J. Cell Biol. *91*, 923–929. https://doi.org/10.1016/j.ejcb.2012.04.002.
62. Belyy, A., Merino, F., Sitsel, O., and Raunser, S. (2020). Structure of the Lifeact–F-actin complex. PLoS Biol. *18*, e3000925. https://doi.org/10.1371/journal.pbio.3000925.
63. Courtemanche, N., Pollard, T.D., and Chen, Q. (2016). Avoiding artifacts when counting polymerized actin in live cells with Lifeact-fluorescent fusion proteins. Nat. Cell Biol. *18*, 676–683. https://doi.org/10.1038/ncb3351.
64. Kang, H., Bradley, M.J., Elam, W.A., and De La Cruz, E.M. (2013). Regulation of actin by ion-linked equilibria. Biophys. J. *105*, 2621–2628. https://doi.org/10.1016/j.bpj.2013.10.032.
65. Welles, R.M., Sojitra, K.A., Garabedian, M.V., Xia, B., Wang, W., Guan, M., Regy, R.M., Gallagher, E.R., Hammer, D.A., Mittal, J., et al. (2024). Determinants that enable disordered protein assembly into discrete condensed phases. Nat. Chem. *16*, 1062–1072. https://doi.org/10.1038/s41557-023-01423-7.
66. Limozin, L., Bärmann, M., and Sackmann, E. (2003). On the organization of self-assembled actin networks in giant vesicles. Eur. Phys. J. E Soft Matter *10*, 319–330. https://doi.org/10.1140/epje/i2002-10118-9.
67. Miyazaki, M., Chiba, M., Eguchi, H., Ohki, T., and Ishiwata, S. (2015). Cell-sized spherical confinement induces the spontaneous formation of contractile actomyosin rings in vitro. Nat. Cell Biol. *17*, 480–489. https://doi.org/10.1038/ncb3142.
68. Claessens, M.M.a.E., Tharmann, R., Kroy, K., and Bausch, A.R. (2006). Microstructure and viscoelasticity of confined semiflexible polymer networks. Nat. Phys. *2*, 186–189. https://doi.org/10.1038/nphys241.
69. Pollard, T.D. (2007). Regulation of actin filament assembly by Arp2/3 complex and formins. Annu. Rev. Biophys. Biomol. Struct. *36*, 451–477. https://doi.org/10.1146/annurev.biophys.35.040405.101936.
70. Henson, J.H., Yeterian, M., Weeks, R.M., Medrano, A.E., Brown, B.L., Geist, H.L., Pais, M.D., Oldenbourg, R., and Shuster, C.B. (2015). Arp2/3 complex inhibition radically alters lamellipodial actin architecture, suspended cell shape, and the cell spreading process. Mol. Biol. Cell *26*, 887–900. https://doi.org/10.1091/mbc.E14-07-1244.
71. Yang, C., and Svitkina, T. (2011). Filopodia initiation: focus on the Arp2/3 complex and formins. Cell Adh. Migr. *5*, 402–408. https://doi.org/10.4161/cam.5.5.16971.
72. Firat-Karalar, E.N., and Welch, M.D. (2011). New mechanisms and functions of actin nucleation. Curr. Opin. Cell Biol. *23*, 4–13. https://doi.org/10.1016/j.ceb.2010.10.007.
73. Zuchero, J.B., Coutts, A.S., Quinlan, M.E., Thangue, N.B.L., and Mullins, R.D. (2009). p53-cofactor JMY is a multifunctional actin nucleation factor. Nat. Cell Biol. *11*, 451–459. https://doi.org/10.1038/ncb1852.
74. Dominguez, R., and Holmes, K.C. (2011). Actin structure and function. Annu. Rev. Biophys. *40*, 169–186. https://doi.org/10.1146/annurev-biophys-042910-155359.
75. Dominguez, R. (2010). Structural insights into *de novo* actin polymerization. Curr. Opin. Struct. Biol. *20*, 217–225. https://doi.org/10.1016/j.sbi.2009.12.012.
76. Quinlan, M.E., Heuser, J.E., Kerkhoff, E., and Mullins, R.D. (2005). Drosophila Spire is an actin nucleation factor. Nature *433*, 382–388. https://doi.org/10.1038/nature03241.
77. Ahuja, R., Pinyol, R., Reichenbach, N., Custer, L., Klingensmith, J., Kessels, M.M., and Qualmann, B. (2007). Cordon-bleu is an actin nucleation factor and controls neuronal morphology. Cell *131*, 337–350. https://doi.org/10.1016/j.cell.2007.08.030.
78. Bieling, P., Hansen, S.D., Akin, O., Li, T.D., Hayden, C.C., Fletcher, D.A., and Mullins, R.D. (2018). WH2 and proline-rich domains of WASP-family proteins collaborate to accelerate actin filament elongation. EMBO J. *37*, 102–121. https://doi.org/10.15252/embj.201797039.
79. Breitsprecher, D., Kiesewetter, A.K., Linkner, J., Urbanke, C., Resch, G.P., Small, J.V., and Faix, J. (2008). Clustering of VASP actively drives processive, WH2 domain-mediated actin filament elongation. EMBO J. *27*, 2943–2954. https://doi.org/10.1038/emboj.2008.211.
80. Brühmann, S., Ushakov, D.S., Winterhoff, M., Dickinson, R.B., Curth, U., and Faix, J. (2017). Distinct VASP tetramers synergize in the processive elongation of individual actin filaments from clustered arrays. Proc. Natl. Acad. Sci. USA *114*, E5815–E5824. https://doi.org/10.1073/pnas.1703145114.
81. Popp, D., Yamamoto, A., and Maéda, Y. (2007). Crowded surfaces change annealing dynamics of actin filaments. J. Mol. Biol. *368*, 365–374. https://doi.org/10.1016/j.jmb.2007.01.087.
82. Andrianantoandro, E., Blanchoin, L., Sept, D., McCammon, J.A., and Pollard, T.D. (2001). Kinetic mechanism of end-to-end annealing of actin filaments1. J. Mol. Biol. *312*, 721–730. https://doi.org/10.1006/jmbi.2001.5005.
83. Clarke, J., Melcher, L., Crowell, A.D., Cavanna, F., Houser, J.R., Graham, K., Green, A.M., Stachowiak, J.C., Truskett, T.M., Milliron, D.J., et al. (2024). Morphological control of bundled actin networks subject to fixed-mass depletion. J. Chem. Phys. *161*, 074905. https://doi.org/10.1063/5.0197269.
84. Hosek, M., and Tang, J.X. (2004). Polymer-induced bundling of F actin and the depletion force. Phys. Rev. E Stat. Nonlin. Soft Matter Phys. *69*, 051907. https://doi.org/10.1103/PhysRevE.69.051907.

85. Holt, M.R., and Koffer, A. (2001). Cell motility: proline-rich proteins promote protrusions. Trends Cell Biol. *11*, 38–46. https://doi.org/10.1016/S0962-8924(00)01876-6.

86. Hwang, T., Parker, S.S., Hill, S.M., Grant, R.A., Ilunga, M.W., Sivaraman, V., Mouneimne, G., and Keating, A.E. (2022). Native proline-rich motifs exploit sequence context to target actin-remodeling Ena/VASP protein ENAH. eLife *11*, e70680. https://doi.org/10.7554/eLife.70680.

87. Case, L.B., Ditlev, J.A., and Rosen, M.K. (2019). Regulation of transmembrane signaling by phase separation. Annu. Rev. Biophys. *48*, 465–494. https://doi.org/10.1146/annurev-biophys-052118-115534.

88. Zeno, W.F., Baul, U., Snead, W.T., DeGroot, A.C.M., Wang, L., Lafer, E.M., Thirumalai, D., and Stachowiak, J.C. (2018). Synergy between intrinsically disordered domains and structured proteins amplifies membrane curvature sensing. Nat. Commun. *9*, 4152. https://doi.org/10.1038/s41467-018-06532-3.

STAR★METHODS

KEY RESOURCES TABLE

REAGENT or RESOURCE	SOURCE	IDENTIFIER
Bacterial and virus strains		
Escherichia coli BL21	NEB	cat. no. C2527H
Escherichia coli DH5 alpha	NEB	N/A
Chemicals, peptides, and recombinant proteins		
Latrunculin A	Cayman Chemical	Item No.10010630
Phalloidin iFluor 594	Abcam	ab176757
EDTA Free Protease Inhibitor Tablets	Roche	cat#05056489001
Ni-NTA agarose resin	Qiagen	cat # 30230
Alexa Fluor 647 maleimide	Thermo Fischer	A20347
Atto 594 maleimide	Sigma Aldrich	08717-1mg-F
Atto 488 NHS Ester	AAT Bioquest	2815
mPEG SVA	Laysan Bio	mPEG-SVA-5000-1G
Pol-L-Lysine	Sigma Aldrich	P2658-100MG
Rabbit Muscle Actin	Cytoskeleton	AKL95-B
Tris(2-carboxyethyl)phopshine (TCEP)	Sigma Aldrich	646547-10X1ML
KLD Enzyme Mix	New England Biolabs	M0554S
Hellmanex III	Sigma Aldrich	Z805939
Critical commercial assays		
Qiagen Miniprep Kit	Qiagen	27104
Phusion High Fidelity PCR Kit	New England Biolabs	E0553S
Oligonucleotides		
mVASP.FOR	Graham et al.[13]	GCTCCAGTTAGTACTCGGACCTACAGAGGG
mVASP.REV	Graham et al.[13]	GTCCGAGTACTAACTGGAGCTGGGCGTG
VASPΔEVH1.FOR	Graham et al.[13]	GACTAAGCGGCCGCGAAGGAGGTGGGCCCC
VASPΔEVH1.REV	Graham et al.[13]	GACTAAGCGGCCGCCTTTACATTTGGA TCCCTGGAAGTACAG
VASP mut-GAB.FOR	Graham et al.[13]	GCCAAACTCGAGGAAGTCAGCAAGCAGG
VASP mut-GAB.REV	Graham et al.[13]	GCTGACTTCCTCGAGTTTGGCTCCAGCAATAG
VASP mut-FAB vector.FOR	Graham et al.[13]	CAGCACAACCTTGCCAAGG
VASP mut-FAB vector.REV	Graham et al.[13]	AATAGCTGCG GCCAGGCC
Eps15-Lifeact.FOR	This paper	TTCGAGAGCATCAGCAAGGAAGAGTGA GGATCCGAATTCGAGCTCC
Eps15-Lifeact.REV	This paper	CTTCTTGATCAGGTCGGCCACGCCCATT GCTTCTGATATCTCAGATTTGCTGAGTG
Software and algorithms		
Cytosim code for modeling figures	This paper	https://doi.org/10.5281/zenodo.14522973
Cytosim	https://gitlab.com/f-nedelec/cytosim	N/A
Origin	OriginLab	v 2024b
ImageJ (FIJI)	Image J	https://doi.org/10.1038/nmeth.2019
Inkscape	Inkscape	v1.3.2

EXPERIMENTAL MODEL AND STUDY PARTICIPANT DETAILS

Plasmid DNA was amplified in *Escherichia coli* DH5α in 2xYT media grown at 37C overnight. The recombinant proteins used in these experiments were produced in *Escherichia coli* BL21 strain, grown until OD600 reaches 0.6∼0.9, and then induced with isopropyl b-D-1- thiogalactopyranoside (IPTG). See the method details section for specific growth conditions for each protein.

METHOD DETAILS

Plasmids

A pET vector encoding the 'cysteine light' variant of human VASP (pET-6xHis-TEV-KCK-VASP(CCC-SSA)) was a gift from Scott Hansen. All VASP mutants were generated using this plasmid as a template, as previously described.[13] Briefly, monomeric VASP (mVASP) was generated using site-directed mutagenesis to introduce a stop codon after amino acid 339 to truncate VASP and remove its tetramerization domain. ΔEVH1 VASP was generated using PCR to delete the EVH1 domain (amino acids 1-113) before recircularization through restriction enzyme digestion and ligation. pET-6xHis-TEV-KCK-VASP-mutGAB was generated by site-directed mutagenesis to mutate residues RK236, 237EE. pET-6xHis-TEV-KCK-VASP-mutFAB was generated using Gibson assembly, with the mutations in the FAB site KR275, 276EE, K278E, K280E included as a gene fragment from Integrated DNA Technologies with the sequence GGCCTGGCCGCAGCTATTGCTGGAGCCAAACTCAGGAAAGTCAGCAAG CAGGAGGAGGCCTCAGGGGGGCCCACAGCCCCCAAAGCTGAGAGTGGTCGAAGCGGAGGTGGGGGACTCATGGAAGAGATGA ACGCCATGCTGGCCGAGGAAGAGGAAGCCACGCAAGTTGGGGAGAAAACCCCCAAGGATGAATCTGCCAATCAGGAGGAGCCA GAGGCCAGAGTCCCGGCCCAGAGTGAATCTGTGCGGAGACCCTGGGAGAAGAACAGCACAACCTTGCCAAGG.[13,15]

The vector encoding mini-Lpd (his-Z-EGFP-LZ-Lpd(aa850-1250)) and monomeric-mini-Lpd (his-EGFP-Lpd(aa850-1250)) were gifts from Scott Hansen.[25]

pET28a 6×His-Eps15 (FL), encoding H. sapiens Eps15, was a gift from Tomas Kirchhausen. Lifeact addition to Eps15 FL was done through site-directed mutagenesis. PCR was done to introduce the Lifeact sequence to the c-terminal end of Eps15 which was followed by the addition of the PCR product to a KLD enzyme mix for template removal, phosphorylation, and ligation into a re-circulated plasmid.

All oligonucleotides used for cloning these constructs are listed in the key resources table.

Protein Purification

The mini-Lpd (his-Z-EGFP-LZ-Lpd(aa850-1250)) and monomeric-mini-Lpd (his-EGFP-Lpd(aa850-1250)) were transformed into BL21 (NEB, cat. No. C2527H) and grown at 30 °C to an OD of 0.8. The bacteria were then cooled to 12°C and induced for 24 hours with 1mM IPTG. The rest of the protocol was performed at 4 °C. Cells were pelleted from a 2L culture by centrifugation at 4,785g (5,000 rpm in Beckman JLA-8.100) for 20 min. Pellets were resuspended in 100mL of lysis buffer (50mM sodium phosphate pH 8.0, 300mM NaCl, 10mM imidazole, 0.5mM TCEP, 0.2% Triton X100, 10% glycerol, 1mM PMSF, and EDTA free protease inhibitor tablets (1 tablet per 50mL) (Roche cat# 05056489001)) followed by sonication on ice for 4x2000J with amplitude at 10 (Sonicator Qsonica LLC, Q700). The lysate was clarified by centrifugation at 48,384g (20,000 rpm in Beckman JA25.50) for 30 min at 4 °C before being applied to a 10mL bed volume Nickel nitrilotriacetic acid (Ni-NTA) agarose (Qiagen, cat. no. 30230) column, and washed with 10 column volumes (CVs) of lysis buffer to which imidazole had been added to a final concentration of 20mM. The column was then washed with 5 column volumes of lysis buffer containing 20 mM Imidazole but lacking Triton-X100 and protease inhibitor tablets. The protein was eluted with elution buffer (50 mM Tris-HCl, pH 7.5, 300mM NaCl, 10% glycerol, 400mM imidazole, 1mM TECP, 1mM PMSF, and EDTA-free protease inhibitor tablets (1 tablet per 50mL). The protein was concentrated using Amicon Ultra-15, 30K MWCO (Millipore: Cat#UFC903024) to 5 mL, and clarified by ultracentrifugation for 5min at 68,000 x g (40,000 rpm with Beckman optimal MAX-E Ultracentrifuge and TLA100.3 rotor). The protein was further purified by size exclusion chromatography with Superose 6, and ion exchange chromatography with SP Sepharose Fast Flow (GE Healthcare, Cat#17-0729-01), and stored as liquid nitrogen pellets at -80°C.

The pET-His-KCK-VASP(CCC-SSA) plasmid was transformed into Escherichia coli BL21(DE3) competent cells (NEB, cat. no. C2527). Cells were grown at 30 °C to an optical density (OD) of 0.8. Protein expression was performed as described previously with some alteration.[15] Expression of VASP was induced with 0.5 mM isopropylthiogalactoside (IPTG), and cells were shaken at 200 rpm at 12 °C for 24 h. The rest of the protocol was carried out at 4 °C. Cells were pelleted from 2 L cultures by centrifugation at 4,785g (5,000 rpm in Beckman JLA-8.100) for 20 min. Cells were resuspended in 100 mL lysis buffer (50 mM sodium phosphate pH 8.0, 300 mM NaCl, 5% glycerol, 0.5 mM TCEP, 10 mM imidazole, 1 mM phenylmethyl sulphonyl fluoride (PMSF)) plus EDTA-free protease inhibitor tablets (1 tablet per 50 mL, Roche, cat. no. 05056489001), 0.5% Triton-X100, followed by homogenization with a dounce homogenizer and sonication (4 × 2,000 J). The lysate was clarified by ultracentrifugation at 125,171g (40,000 rpm in Beckman Ti45) for 30 min. The clarified lysate was then applied to a 10 mL bed volume Nickel nitrilotriacetic acid (Ni-NTA) agarose (Qiagen, cat. no. 30230) column, washed with 10 column volumes of lysis buffer plus EDTA-free protease inhibitor tablets (1 tablet per 50 mL), 20 mM imidazole, 0.2% Triton X-100, followed by washing with 5×CV of lysis buffer plus 20 mM imidazole. The protein was eluted with elution buffer (50 mM Tris, pH 8.0, 300 mM NaCl, 5% glycerol, 250 mM imidazole, 0.5 mM TECP, EDTA-free protease inhibitor tablets (1 tablet per 50 mL)). The protein was further purified by size exclusion chromatography with Superose 6 resin. The resulting purified KCK-VASP was eluted in storage buffer (25 mM HEPES pH 7.5, 200 mM NaCl, 5% glycerol, 1 mM EDTA, 5 mM DTT). Single-use aliquots were flash-frozen using liquid nitrogen and stored at −80 °C until the day of an experiment. The his-tagged VASP mutants were purified using the same protocol as above as indicated or with the following modifications: His-KCK-VASPΔTet: no modifications. GST-KCK-VASPΔEVH1 was purified using the same protocol as above but with the following buffer modifications: The lysis buffer was 20 mM Tris pH 8.5, 350 mM NaCl, 5% glycerol, 5 mM EDTA, 5 mM DTT, and 1 mM PMSF. The storage buffer was 25 mM HEPES, pH 7.5, 200 mM NaCl, 5% glycerol, 1 mM EDTA, and 5 mM DTT.

For KCK-VASP-mutGAB, the following buffers were used: lysis buffer of 20 mM Tris pH 8.5, 300 mM NaCl, 10 mM imidazole, 5% glycerol, 0.5 mM TCEP, 0.5% Triton X-100, 1 mM PMSF, and complete EDTA-free protease inhibitor cocktail tablet (1 tablet per 50 mL). The protein-bound resin was washed with 100 mL of 20 mM Tris pH 8.5, 300 mM NaCl, 10 mM imidazole, 5% glycerol, 0.5 mM TCEP, 0.2% Triton X-100, 1 mM PMSF and complete EDTA free protease inhibitor cocktail tablet (1 tablet per 50 m), then washed with 50 mL of 20 mM Tris pH8.5, 300 mM NaCl, 10 mM imidazole, 5% glycerol, 0.5 mM TCEP and 1 mM PMSF. The elution buffer was 50 mM Tris pH 8.5, 300 mM NaCl, 5% glycerol, 250 mM imidazole, and 0.5 mM TCEP. The TEV digestion buffer was 50 mM Tris pH 8.0, 200 mM NaCl, 5% glycerol, 0.5 mM EDTA, and 1 mM DTT. The gel filtration and storage buffer were 25 mM HEPES, pH 7.5, 200 mM NaCl, 5% glycerol, 1 mM EDTA, and 1 mM DTT. For KCK-VASP-mutFAB, the following conditions were used: lysis buffer of 20 mM Tris pH 8.0, 300 mM NaCl, 10 mM imidazole, 10 mM potassium phosphate pH 8.0, 10% glycerol, 0.5 mM TCEP, 0.5% Triton X-100, 1 mM PMSF and complete EDTA-free protease inhibitor cocktail tablet (1 tablet per 50 mL). The protein-bound resin was washed with 100 mL of 20 mM Tris pH 8.0, 300 mM NaCl, 10 mM imidazole, 10 mM potassium phosphate pH 8.0, 10% glycerol, 0.5 mM TCEP, 0.2% Triton X-100, 1 mM PMSF and complete EDTA-free protease inhibitor cock tail tablet (1 tablet per 50 mL), then washed with 50 mL of 20 mM Tris pH8.0, 300 mM NaCl, 10 mM imidazole, 10 mM potassium phosphate pH 8.0, 10% glycerol, 0.5 mM TCEP and 1 mM PMSF. The elution buffer was 50 mM Tris pH 8.0, 300 mM NaCl, 2 mM potassium phosphate pH 8.0, 10% glycerol, 400 mM imidazole, and 0.5 mM TCEP. The TEV digestion buffer was 50 mM Tris pH 8.0, 200 mM NaCl, 10% glycerol, 2 mM potassium phosphate pH 8.0, 0.5 mM EDTA, and 1 mM DTT. The gel filtration and storage buffer was 20 mM Tris pH 8.5, 200 mM NaCl, 10 mM potassium phosphate pH 8.0, 10% glycerol, 1 mM EDTA, and 1 mM DTT.

Full-length Eps15 and Eps15-Lifeact were expressed as N-terminal 6x-His-tagged constructs in BL21(DE3) *E. Coli* cells. Cells were grown in 2xYT medium for 3-4 hours at 30 ^{o}C to an optical density at 600 nm of 0.6-0.9, cooled for 1 hour, and then protein expression was induced with 1 mM IPTG at 12^{o}C for 20-30 hours. Cells were collected, and bacteria were lysed in a lysis buffer using homogenization and probe sonication. Lysis buffer was 50 mM Tris-HCl, pH 8.0, 300 mM NaCl, 5 mM imidazole, 10 mM β-mercaptoethanol or 5 mM TCEP, 1 mM PMSF, 0.2% Triton X-100 and 1x Roche or Pierce complete EDTA-free protease inhibitor cocktail tablet per 50 mL buffer. Proteins were incubated with Ni-NTA Agarose (Qiagen 30230) resin, followed by extensive washing with 10 column volumes, then eluted from the resin in 50 mM Tris-HCl, pH 8.0, 300 mM NaCl, 200 mM imidazole, 10 mM β-mercaptoethanol or 5 mM TCEP, 1 mM PMSF, and 1× Roche or Pierce complete EDTA-free protease inhibitor cocktail tablet. The protein was then further purified by gel filtration chromatography using a Superose 6 column equilibrated with 20 mM Tris-HCl, pH 8.0, 150 mM NaCl, 1 mM EDTA, and 5 mM DTT. Purified proteins were concentrated using Amicon Ultra-15 Ultracell-30K centrifugal filter units (Millipore–Sigma), then centrifuged at 100,000 rpm at 4 °C for 10min using a Beckman TLA-120.2 rotor to remove aggregates, and stored either in small aliquots or as liquid nitrogen pellets at −80 °C.

Protein labeling

The VASP and VASP mutants used in these studies is a previously published 'cysteine light' mutant that replaced the three endogenous cysteines with two serines and an alanine. A single cysteine was then introduced at the N-terminus of the protein to allow selective labeling with maleimide dyes. This mutant was found to function in an indistinguishable manner from the wild-type proteins.[14] Thus, VASP and its mutants were labeled at the N-terminal cysteine using maleimide-conjugated dyes. VASP was buffer exchanged into 20 mM Tris (pH 7.4) 150 mM NaCl buffer to remove DTT from the storage buffer and then incubated with a three-fold molar excess of dye for two hours at room temperature. Free dye was then removed by applying the labeling reaction to a Zeba Dye and Biotin removal size exclusion column (Thermo Fischer Scientific) equilibrated with buffer containing 20 mM Tris pH 7.4, 150 mM NaCl, and 5 mM TCEP.

Monomeric actin was labeled using maleimide-conjugated dyes. Dyes were incubated with G-actin at a 2-fold molar excess for 2 hours at room temperature before being separated from the labeled protein by applying the labeling reaction to a spin column packed with Sephadex G-50 Fine DNA Grade (GE Healthcare GE17-0573-01) hydrated with A buffer (5 mM Tris-HCL (pH 8), 0.2 mM ATP and 0.5 mM DTT pH 8). The labeled protein was then centrifuged at 100,000 x G for 10 min at 4 degrees Celsius to remove aggregates before being flash-frozen in single-use aliquots.

Eps15 and Eps15-Lifeact were labeled using amine-reactive NHS-ester dyes at a 3-fold molar excess of dye before free dye was removed by applying the labeling reaction to a Zeba Dye and Biotin removal size exclusion column (Thermo Fischer Scientific) equilibrated with buffer containing 20 mM Tris (pH 7.4), 150 mM NaCl, and 5 mM TCEP.

Protein condensate formation and actin filament assembly

Condensates composed of VASP, VASP mutants, mini-Lpd, monomer mini-Lpd, Eps15, and Eps15-Lifeact were formed by mixing the given concentration of protein (see text) with 3% (w/v) PEG 8000 in 20 mM Tris pH 7.4, 5 mM TCEP, and the given concentration of NaCl (50 mM for mini-Lpd/monomer mini-Lpd and 150 mM for mini-Lpd + VASP, VASP, VASP mutants, Eps15, or Eps15-Lifeact). PEG was added last to induce condensate formation after the protein was evenly dispersed in the solution. For condensates consisting of both mini-Lpd and VASP, formed in the absence of PEG, the only difference was that PEG was not added to the mix. All protein concentrations listed are the monomeric concentrations.

For actin assembly assays within condensates, condensates were formed for ten minutes (with time starting after PEG addition) and then G-actin was added to the condensate solution and allowed to assemble for 15 minutes before imaging. For phalloidin-actin assays, unlabelled G-actin was added to pre-formed protein condensates and allowed to assemble for 10 min. Phalloidin-iFluor594 was then added to stain filamentous actin for 10 min before imaging. For assays that included Latrunculin, 5 μM Latrunculin A was

added to the pre-formed protein condensates and mixed gently before actin addition. For time-lapse experiments, condensates were imaged immediately after actin addition, rather than waiting for 15 minutes before imaging.

For FRAP experiments, condensates formed from the various proteins were observed in solution at the conditions given in the text. A region within the condensates was bleached and consecutive images were taken every three seconds to monitor fluorescence recovery over time.

Microscopy

Samples were prepared for microscopy in 3.5mm or 5mm diameter wells formed using biopsy punches to create holes in 1.6 mm thick silicone gaskets (Grace Biolabs) on Hellmanex III cleaned, no. 1.5 glass coverslips (VWR). Coverslips were passivated using poly-L-lysine conjugated PEG chains (PLL-PEG). To prevent evaporation during imaging, an additional small coverslip was placed on top of the gasket to seal the well. Fluorescence microscopy was done using an Olympus SpinSR10 spinning disk confocal microscope with a Hamamatsu Orca Flash 4.0V3 Scientific CMOS camera. FRAP was done using the Olympus FRAP unit 405 nm laser.

PLL- PEG was prepared as described previously with minor alterations.[88] Briefly, amine-reactive mPEG succinimidyl valerate was conjugated to poly-L-lysine at a molar ratio of 1:5 PEG to PLL. The conjugation reaction takes place in 50mM sodium tetraborate solution pH 8.5 and is allowed to react overnight at room temperature while continuously stirring. The final product is then buffer exchanged to PBS pH 7.4 using 7000 MWCO Zeba spin desalting columns (Thermo Fisher) and stored at 4 °C.

Image Analysis

Image J was used to quantify the distribution of condensate characteristics. Specifically, condensates were selected using thresholding in the brightest channel and shape descriptors (i.e., diameter, aspect ratio, etc.), and protein fluorescent intensities were measured using the built-in analyze particles function. For aspect ratio analysis condensates that had come into contact with other condensates were removed from the analysis to avoid any skewing of data from misrepresentation of single condensate deformation.

FRAP data were analyzed using ImageJ where fluorescence recovery over time was measured and then normalized to the maximum pre-bleach intensity. Recovery was measured for condensates of similar diameters and photobleached region size.

Partitioning data was calculated using the average intensities of the condensed protein phase and the bulk solution, with partitioning defined as the ratio of the intensity inside the condensate to outside the condensate. Images were cropped so that only condensates from the middle ninth of the field of view were analyzed to avoid any error from potential non-uniform illumination across the imaging field.

Modeling

Detailed methods and parameters for the modeling component of this work can be found in the Methods S1 and Tables S1 and S2.

QUANTIFICATION AND STATISTICAL ANALYSIS

Statistical details of experiments can be found in the corresponding figure captions, including replicate numbers, *n* values, significance tests used, and significance thresholds.

Developmental Cell, Volume *60*

Supplemental information

Liquid-like condensates that bind actin promote assembly and bundling of actin filaments

Caleb Walker, Aravind Chandrasekaran, Daniel Mansour, Kristin Graham, Andrea Torres, Liping Wang, Eileen M. Lafer, Padmini Rangamani, and Jeanne C. Stachowiak

Supplemental Material

Supplemental Tables

Table S1: Table of parameters required to set up the actin model in Cytosim. This set of parameters is common to all the simulations conducted for this study. Related to STAR methods.

Parameter	Value	Notes/Reference
Total time	600 s	
Time step	0.002 s	
Condensate viscosity	0.5 pN·s/μm^2	500x water; Chosen based on protein condensate viscosities[S1]
Boundary		
Shape	Sphere	
Radius	1 μm	
Boundary repulsion stiffness	200 pN/μm for actin filaments; 100 pN/μm for crosslinking molecules	This specifies the spring stiffness that acts on the discretized points of each actin filament and crosslinking molecule if the point lies outside the specified boundary. The force on each point is dependent on the distance that it lies beyond the confines of the boundary.
Actin filaments		
Segmentation length L_{seg}	0.1 μm (100 nm)	
Maximum length	2πR μm	
Polymerization rate k_{grow}	0.0103 μm/s	Only plus (+) end extension is allowed. This rate is calculated by assuming a final filament length of 2π μm at 600 s.
Brownian ratchet force for polymerization	10 pN	[S2]
Actin flexural rigidity k_{bend}	0.075 pN·μm^2	[S3]
Actin steric repulsion k_{steric}	Radius 3.5 nm Stiffness 1.0 pN/μm	Chosen to ensure the observation of ring structures within the kinetic parameters used in this study as determined from a previous study.[S4]
Bivalent crosslinkers (mini-Lpd)		
Radius	30 nm	
Diffusion rate	10 μm^2/s	

Concentration of dimers	0.40 μM [1000 dimers]	
Actin-binding rate (Ring Conditions)	10.0 (1/s)	Determined from VASP and mini-Lpd simulations.
Actin-binding rate (Shell Conditions)	0.1 (1/s)	Determined from VASP and mini-Lpd simulations.
Actin-binding distance	30 nm	
Actin-binding valency	2	Each spherical molecule approximates a mini-Lpd dimer.
Zero-force actin-unbinding rate (Ring and Shell Conditions)	1.0 (1/s)	Determined from VASP and mini-Lpd simulations.
Actin-unbinding force	10 pN	Typical values for passive crosslinkers.[S5]
mini-Lpd steric repulsion	Radius 30 nm Stiffness 1.0 pN/μm	Chosen to ensure the observation of ring structures within the kinetic parameters used in this study as determined from a previous study on tetramers.[S4]
Tetravalent crosslinkers (VASP)		
Radius	30 nm	
Diffusion rate	10 $\mu m^2/s$	
Concentration of tetramers	0.40 μM [1000 tetramers]	
Actin-binding rate (Ring Conditions)	10.0 (1/s)	Determined from VASP and mini-Lpd simulations.
Actin-binding rate (Shell Conditions)	0.1 (1/s)	Determined from VASP and mini-Lpd simulations.
Actin-binding distance	30 nm	
Actin-binding valency	4	Each spherical molecule approximates a VASP tetramer.
Zero-force actin-unbinding rate (Ring and Shell Conditions)	1.0 (1/s)	Determined from VASP and mini-Lpd simulations.
Actin-unbinding force	10 pN	Typical values for passive crosslinkers.[S5]
VASP steric repulsion	Radius 30 nm Stiffness 10 pN/μm	Chosen to ensure the observation of ring structures within the kinetic parameters used in this study as determined from a previous study on tetramers.[S4]
Monovalent actin binders for dynamic dimerization and dynamic multimerization models (mini-Lpd monomers)		
Radius	30 nm	

Diffusion rate	10 $\mu m^2/s$	
Concentration of monomers	0.79 μM [2000 monomers]	
Actin-binding rate (Ring Conditions)	10.0 (1/s)	Determined from VASP and mini-Lpd simulations.
Actin-binding rate (Shell Conditions)	0.1 (1/s)	Determined from VASP and mini-Lpd simulations.
Actin-binding distance	30 nm	
Actin-binding valency	1	Each spherical molecule approximates a mini-Lpd monomer.
Zero-force actin-unbinding rate (Ring and Shell Conditions)	1.0 (1/s)	Determined from VASP and mini-Lpd simulations.
Actin-unbinding force	10 pN	Typical values for passive crosslinkers.[S5]
mini-Lpd monomer-actin steric repulsion	Radius R_{solid} = 30 nm Stiffness 10 pN/μm	Chosen to ensure the observation of ring structures within the kinetic parameters used in this study as determined from a previous study on tetramers.[S4]
mini-Lpd monomer-monomer binding distance	90 nm ($3R_{solid}$)	This is the distance between the binding site on solid A and the center of solid B. So, if two solids are in contact, depending on the position of the binding site this distance can scale between R_{solid} and $3R_{solid}$, where R_{solid} is the radius of solid.
mini-Lpd monomer-monomer splitting force	10 pN	Used in this study
mini-Lpd monomer-monomer steric repulsion	Radius 30 nm Stiffness 5.0 pN/μm	Chosen empirically to ensure adequate dimerization reactions occur to support the observation of ring structures in **Figure 5**.

Table S2: Additional parameters employed to simulate specific simulations discussed in this paper. Related to STAR Methods.

Parameter	Value	Notes/Reference
Parameters for simulations with mixtures of bivalent and tetravalent crosslinkers (Figure S6)		
Tetravalent: Bivalent crosslinker copy number ratios	{1000:0, 750:250, 500:500, 250:750, 0:1000}	Used in this study
Tetravalent-Bivalent crosslinker copy number kinetic conditions	{Ring-Ring, Ring-Shell, Shell-Ring}	Kinetic conditions considered, values shown in **Table S1**.
Parameters for simulations with bivalent crosslinkers (Figure 4)		
Binding rates $k_{bind}^{mini-Lpd}$	{10^{-3}, 10^{-2}, 10^{-1}, 10^{0}, 10^{+1}} (1/s)	Range determined based on a previous study with tetramers.[S4]
Zero-force actin unbinding rates $k_{unbind}^{mini-Lpd}$	{10^{-3}, 10^{-2}, 10^{-1}, 10^{0}, 10^{+1}} (1/s)	
Parameters for simulations of dynamically dimerizing proteins (Figure 5)		
Monomer-monomer binding valency	1	Chosen to restrict multimer formation to only dimers.
Dimer forming rates $k_{dimer\ form}$	{10^{-3}, 10^{-2}, 10^{-1}, 10^{0}, 10^{+1}} (1/s)	Used in this study
Dimer splitting rates $k_{dimer\ split}$	{10^{-3}, 10^{-2}, 10^{-1}, 10^{0}, 10^{+1}} (1/s)	Used in this study
Parameters for simulations of dynamically multimerizing proteins (Figure S7)		
Monomer-monomer binding valency	2	Chosen to allow for the formation of higher multimeric states.
Multimer forming rates $k_{multimer\ form}$	{10^{-3}, 10^{-2}, 10^{-1}, 10^{0}, 10^{+1}} (1/s)	Used in this study
Multimer splitting rates $k_{multimer\ split}$	{10^{-3}, 10^{-2}, 10^{-1}, 10^{0}, 10^{+1}}(1/s)	Used in this study

Supplemental Figures

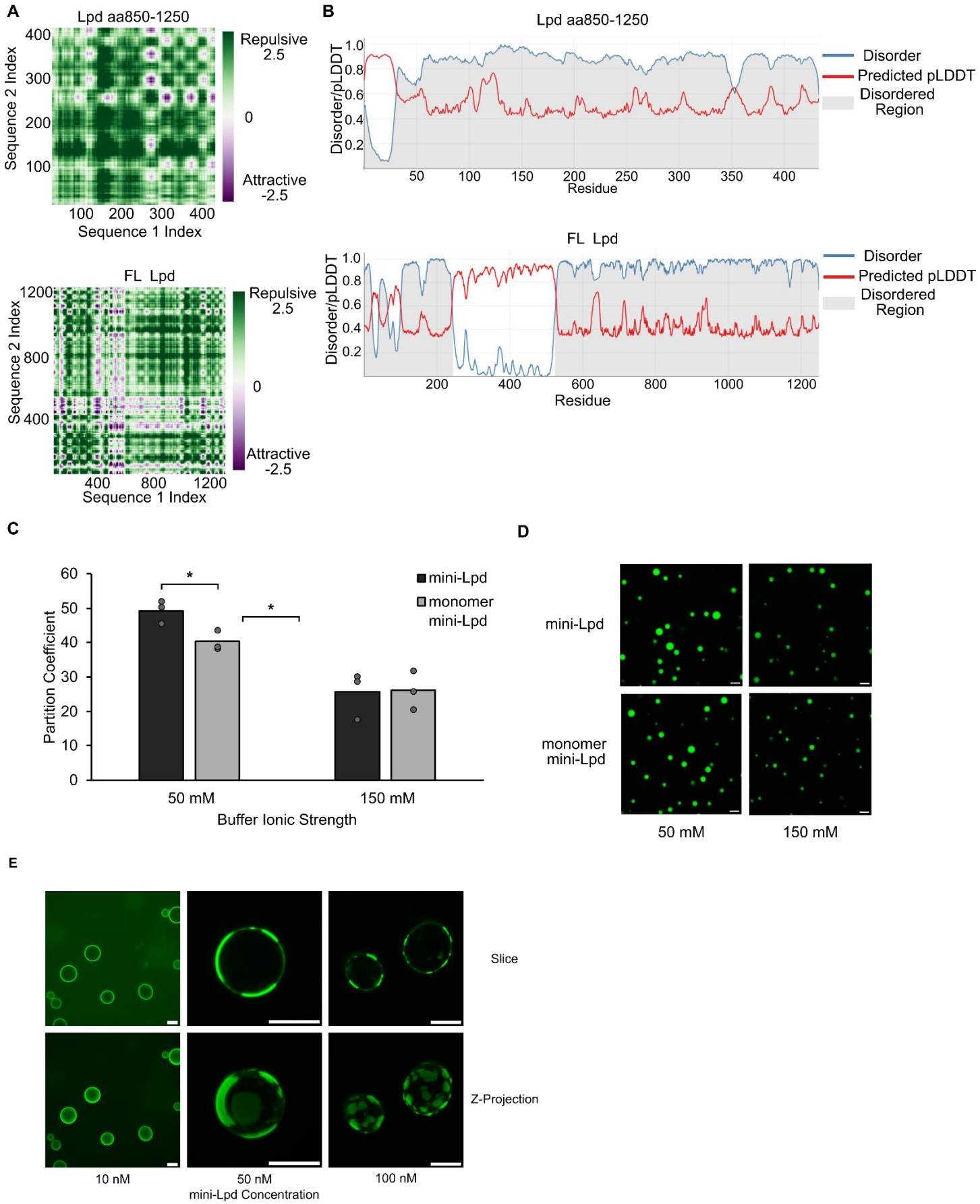

Figure S1: Further analysis of mini-Lpd phase separation. Related to Figure 1. A) Sequence analysis using the FINCHES tool developed by the Holehouse Lab[S6,7] to predict intermolecular interactions of intrinsically disordered regions for (left) amino acids 850-0250 of Lamellipodin that are contained within mini-Lpd and (right) full-length Lamellipodin. Sequence index corresponds to the residues within the protein sequence B) Sequence Analysis using the SPARROW tool developed by the Holehouse Lab[S6] to predict disorder within protein sequences for (top) amino acids 850-0250 of Lamellipodin that are contained within mini-Lpd and (bottom) full-length Lamellipodin. The full-length Lamellipodin protein also scores highly in the phase separation prediction algorithms PSPredictor[S8] and PhasePred[9]. These prediction algorithms use machine learning trained on databases of phase-separating proteins and sequence analysis to give scores (with a max of 1) of the predicted capacity for a sequence to phase separate. Full-length Lamellipodin has scores of 0.9962 from PsPredictor and 0.960 from PhasePred, suggesting a likely capacity to phase separate. C) Comparison of self-partition coefficient of mini-Lpd and monomer mini-Lpd at varying buffer NaCl concentrations. Bars represent the average across three independent experiments with at least three images quantified per experiment. The overlaid gray circles denote the averages for each replicate. One asterisk denotes $p<.05$ using an unpaired, two-tailed t-test on the means of the replicates N=3. D) Representative images of condensates formed from mini-Lpd or monomer mini-Lpd at the given buffer NaCl concentrations. E) Phase separation of mini-Lpd on membrane substrates. Representative images of mini-Lpd recruitment to giant unilamellar vesicles (GUVs) showing (top) a slice and (bottom) z-projections of vesicles. Phase separation on membrane substrates is seen with 50 nM and 100 nM mini-Lpd, but not with 10 nM mini-Lpd. GUVs were made consisting of 84% DOPC, 15% DGS-NiNTA, 1%DP-EG10 biotin, and 0.1% Texas Red- DHPE in buffer consisting of 25mM HEPES pH 7.4, 50mM NaCl, and 5mM TCEP. Scale bars 10 μm.

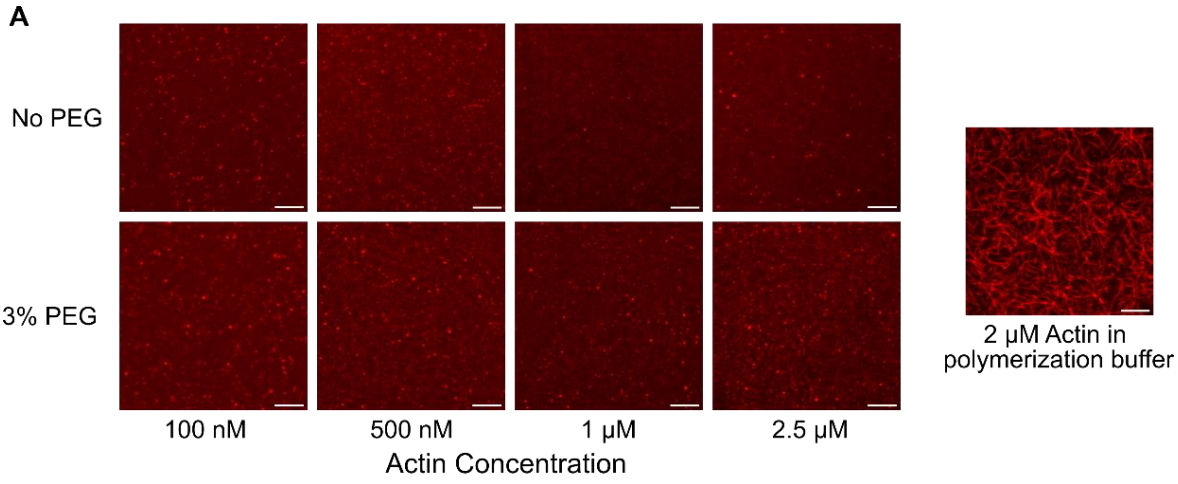
A
No PEG
3% PEG
100 nM
500 nM
1 μM
2.5 μM
Actin Concentration
2 μM Actin in
polymerization buffer

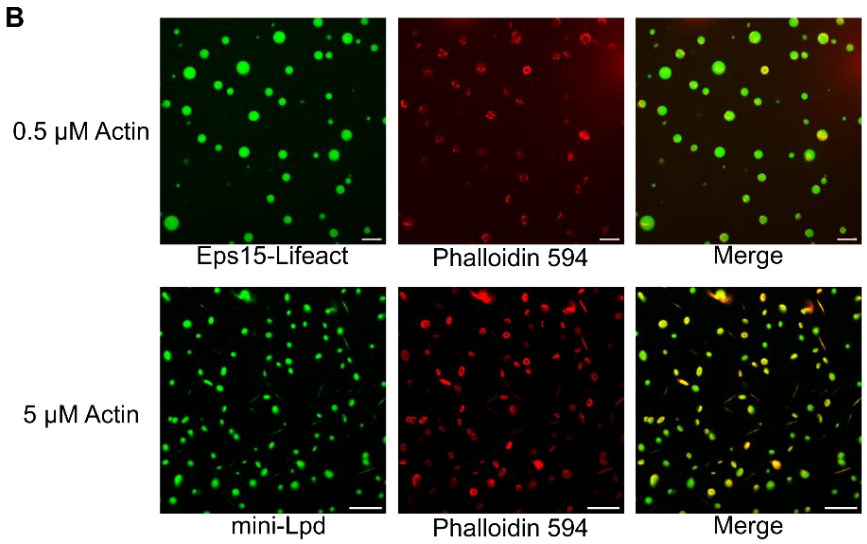
B
0.5 μM Actin
Eps15-Lifeact
Phalloidin 594
Merge
5 μM Actin
mini-Lpd
Phalloidin 594
Merge

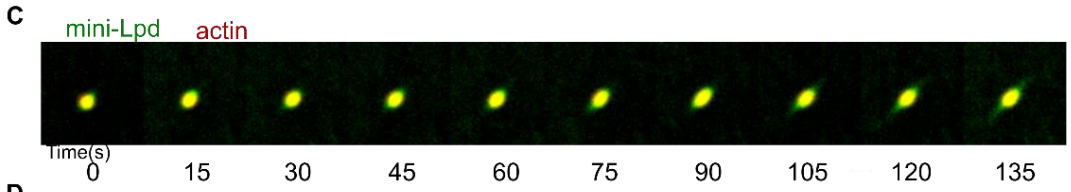
C
mini-Lpd actin
Time(s)
0 15 30 45 60 75 90 105 120 135

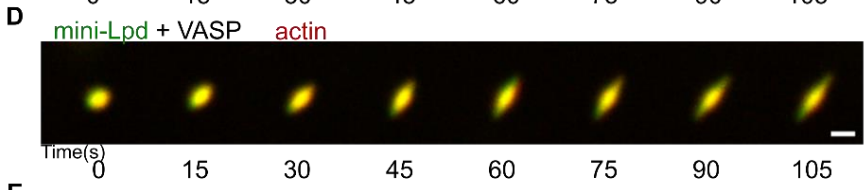
D
mini-Lpd + VASP actin
Time(s)
0 15 30 45 60 75 90 105

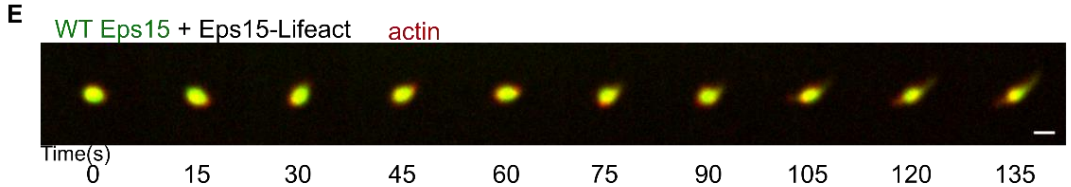
E
WT Eps15 + Eps15-Lifeact actin
Time(s)
0 15 30 45 60 75 90 105 120 135

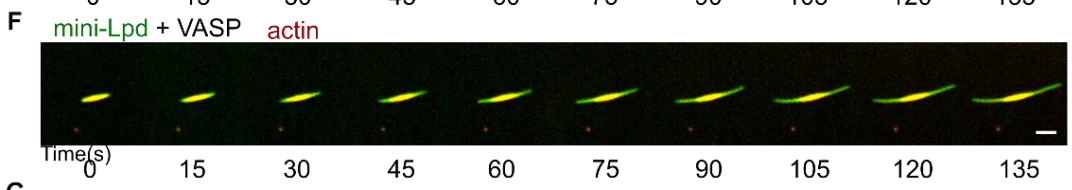
F
mini-Lpd + VASP actin
Time(s)
0 15 30 45 60 75 90 105 120 135

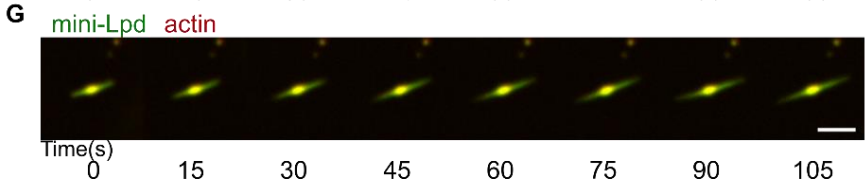
G
mini-Lpd actin
Time(s)
0 15 30 45 60 75 90 105

Figure S2: Actin filament assembly is localized to protein condensates. Related to Figures 3-6. A) Atto 594 fluorescently labeled G-actin fails to spontaneously assemble across the range of actin concentrations in the buffers used for condensate-based experiments (20mM Tris pH 7.4, 150mM NaCl, and 5mM TCEP) in the absence and presence of 3% PEG. (Right) Positive control with buffer containing magnesium chloride, which promotes assembly (10 mM Tris, 2 mM $MgCl_2$, 50 mM KCl, 1 mM ATP, and 0.5 mM DTT) shows actin filament assembly. All scale bars are 5 μm. **B) Top)** Low concentrations of added actin (0.5 μM) show that large actin filaments are absent in the solution surrounding protein condensates, and filaments appear to originate within the condensates. Condensates were formed with 15 μM of a 1:1 ratio of WT Eps15:Eps15-Lifeact in a buffer consisting of 20 mM Tris pH 7.4, 150 mM NaCl, 5 mM TCEP, and 3% PEG. **Bottom)** Conditions with high concentrations of added actin (5 μM) are still devoid of phalloidin-stained actin filament in solution, suggesting the buffer conditions do not support the spontaneous formation of non-diffraction-limited filaments even at high concentrations of actin. Condensates were formed with 5 μM mini-Lpd in a buffer of 20 mM Tris pH 7.4, 150 mM NaCl, 5 mM TCEP, and 3% PEG. **C)** Time-lapse of sphere-to-rod transformation of a condensate formed from mini-Lpd (green) and VASP (unlabeled) upon the addition of 2 μM G-actin (red). Scale bar 1 μm. **D)** Time-lapse of the sphere-to-rod transformation of a mini-Lpd (green) condensate upon the addition of 2μM G-actin (red). Scale bar 1 μm. **E)** Time-lapse of a sphere-to-rod transformation of a condensate formed from a 1:1 ratio of WT Eps15:Eps15-Lifeact (WT Eps15-green, Eps15 Lifeact - unlabeled) upon the addition of 2 μM actin (red). Scale bar 1 μm. **F)** Time-lapse of linear actin filaments (red) within a deformed condensate of mini-Lpd (green) + VASP (unlabeled) elongating over time. Scale bar 1 μm. **G)** Time-lapse of linear actin filaments (red) within a deformed condensate of mini-Lpd (green) elongating over time. Scale bar 1 μm.

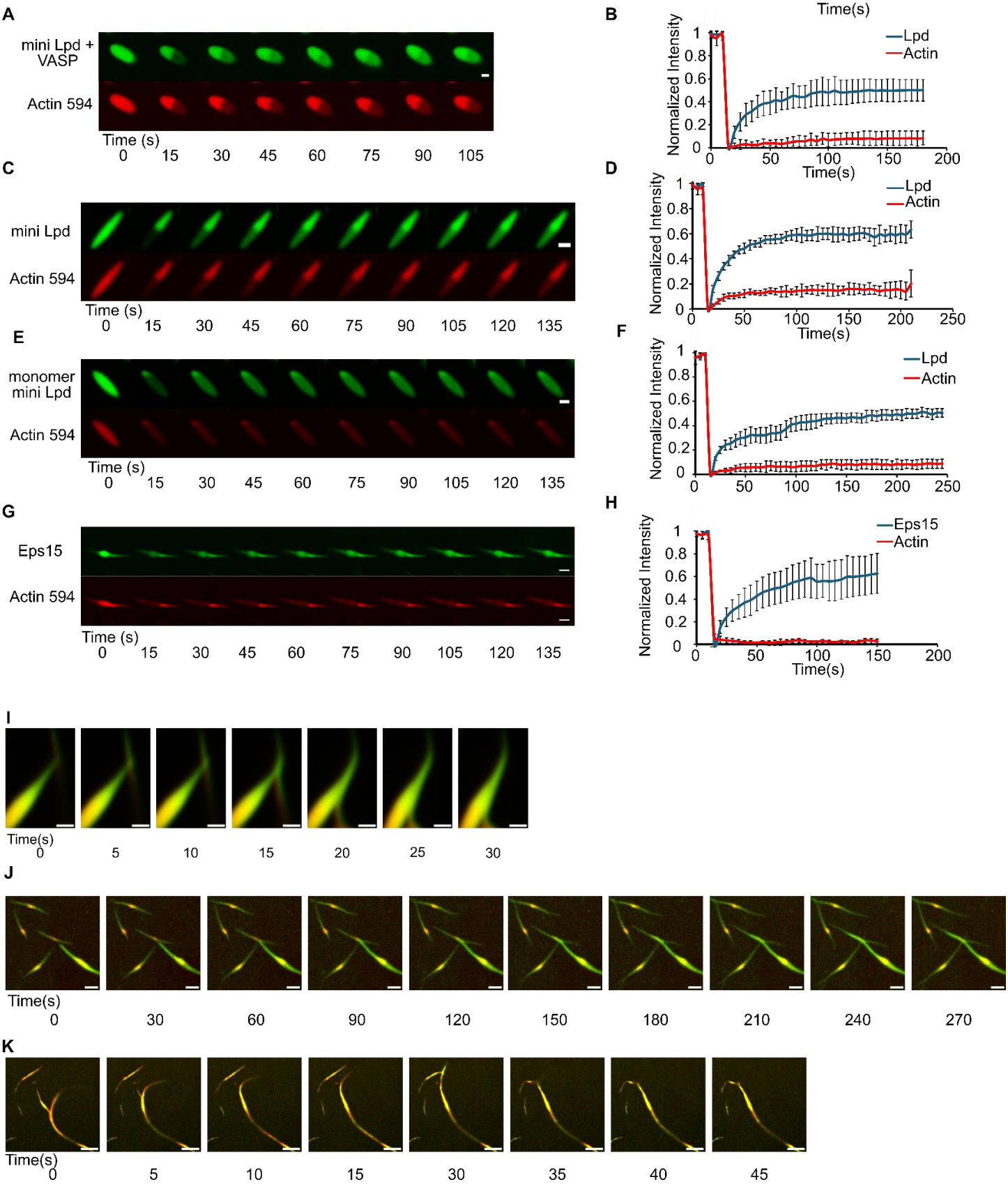
A
mini Lpd + VASP
Actin 594
Time (s)
0 15 30 45 60 75 90 105
B
Time(s)
Normalized Intensity
Lpd
Actin
C
mini Lpd
Actin 594
Time (s)
0 15 30 45 60 75 90 105 120 135
D
E
monomer mini Lpd
Actin 594
F
G
Eps15
Actin 594
H
I
Time(s)
0 5 10 15 20 25 30
J
0 30 60 90 120 150 180 210 240 270
K
0 5 10 15 30 35 40 45

Figure S3: Protein condensates retain liquid-like properties after deformation by actin assembly. Related to Figures 3-6. A) Montage of FRAP recovery of a condensate formed from mini-Lpd (green) and VASP (dark) after actin assembly has led to deformation. Scale bar 1 μm. **B)** Plot of average fluorescence recovery after photobleaching for the mini-Lpd and actin channels. **C)** Montage of FRAP recovery of a condensate formed from mini-Lpd after actin assembly has led to deformation. Scale bar 1 μm. **D)** Plot of average fluorescence recovery after photobleaching for the mini-Lpd and actin channels. **E)** Montage of FRAP recovery of a condensate formed from monomer mini-Lpd after actin assembly has led to deformation. Scale bar 1 μm. **F)** Plot of average fluorescence recovery after photobleaching for the monomer mini-Lpd and actin channels. **G)** Montage of FRAP recovery of a condensate formed from a 1:1 ratio of (green) WT Eps15:Eps15-Lifeact (dark) after actin assembly has led to deformation. **H)** Plot of average fluorescence recovery after photobleaching for the Eps15 and actin channels. Lines in all graphs are the average recovery +/- s.d. at each timepoint for each protein across at least 6 independent samples. **I)** Deformed condensates of mini-Lpd zipper together as they come into contact. Scale bar 1 μm. **J)** Deformed condensates formed from mini-Lpd and VASP zipper together as they come into contact. Scale bar 2 μm. **K)** Deformed condensates formed from a 1:1 ratio of WT Eps15:Eps15-Lifeact zipper together as they come into contact. Scale bar 5 μm.

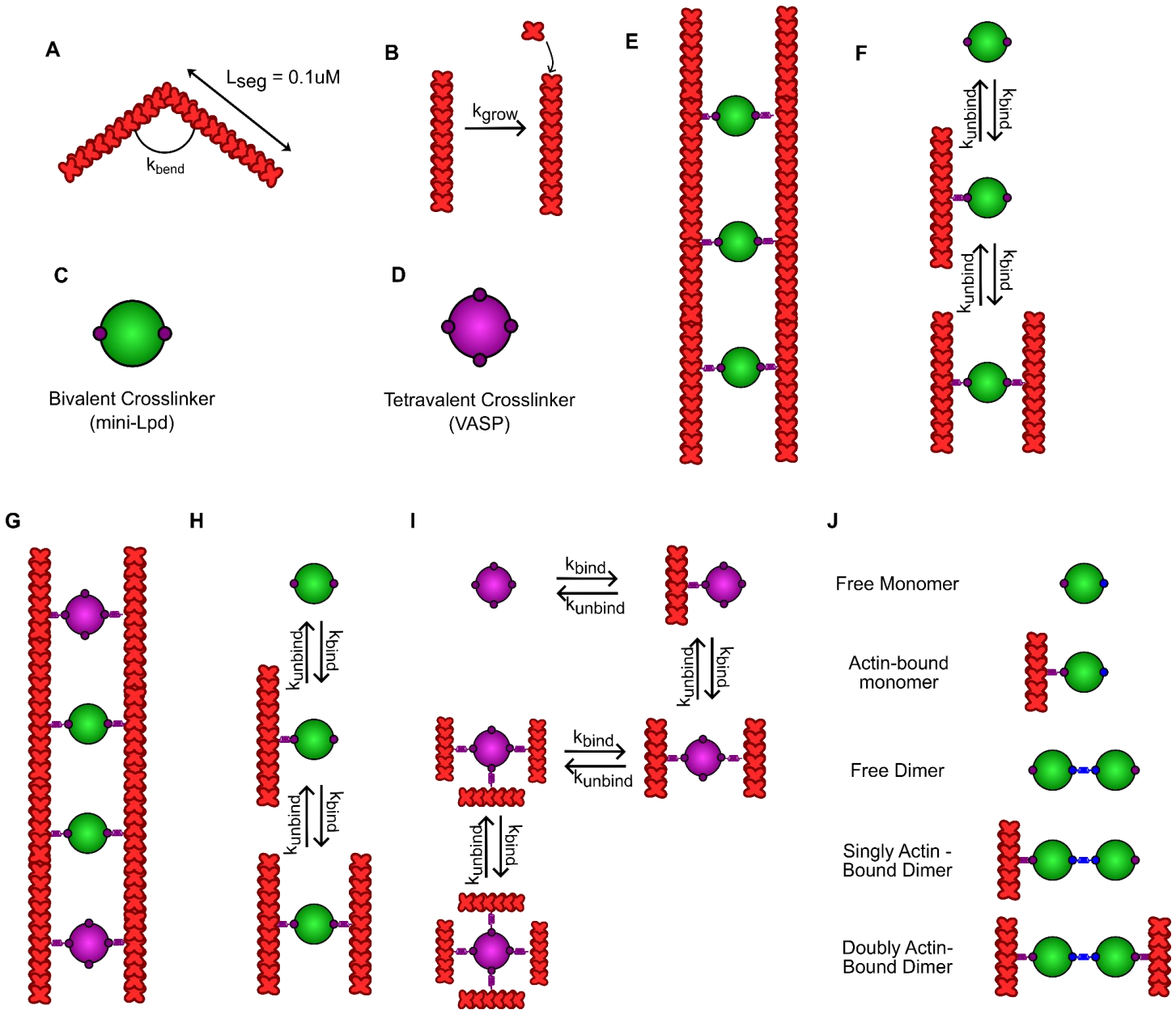

Figure S4: Schematic representation of chemical species and reactions considered. Related to Figures 3-5 A) Actin filaments are modeled as inextensible segments of length L_{seg} that can bend along hinge points based on flexural rigidity k_{bend}. **B)** Filaments in these simulations are allowed to grow deterministically at the rate k_{grow} = 0.0103 μm/s. **C)** Bivalent crosslinkers mimic mini-Lpd dimers and are represented as green-colored solids that have two binding sites (small, purple circles) which can bind and crosslink actin filament. **D)** Tetravalent crosslinkers mimic VASP (in purple) and have four actin-binding sites. **E)** Cartoon representation of two filaments crosslinked by mini-Lpd. **F)** Each of the two actin-binding domains in a dimeric crosslinker binds actin at rate k_{bind} and unbind in a force-sensitive manner with unbinding rate k_{unbind}. **G)** Cartoon representation of two actin filaments crosslinked by both mini-Lpd and VASP molecules. **H, I:** For simulations with mixtures of **H)** mini-Lpd and **I)** VASP, the crosslinking reactions considered are shown. **J)** Cartoon depicting the different possible formations outlined in **Fig 5D.** Please refer to Supporting Information, Tables S1 and S2 for more information on model parameters used in this study.

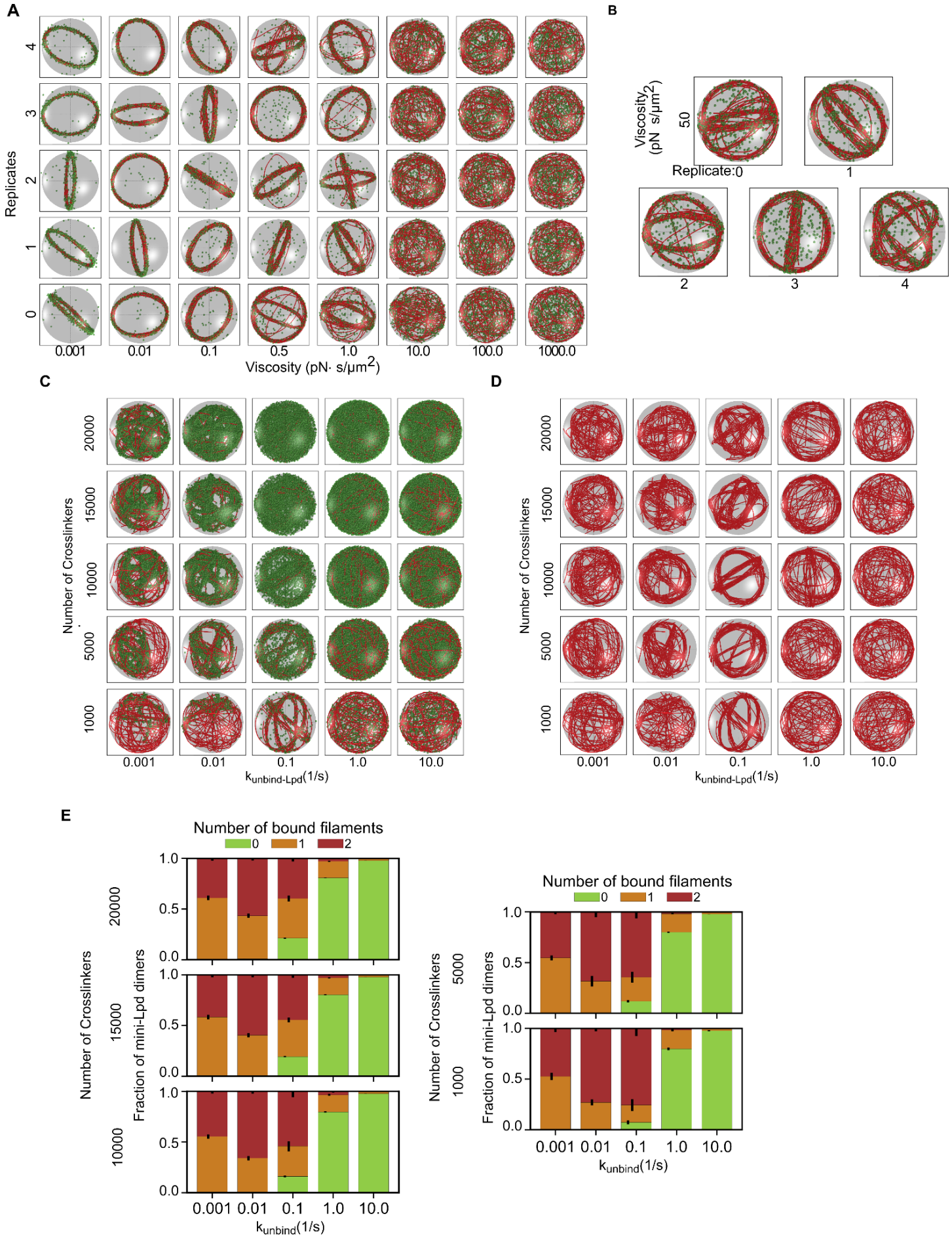

Figure S5: Effect of viscosity and crosslinker number on final actin filament architectures in the model. Related to

Figures 3-5. A) Representative final snapshots (t = 600 s) from multiple replicates ($N_{replicates}$ = 5, shown along the y-axis) of simulations with varied viscosity (varied along the x-axis) within spherical condensates (R = 1 μm) containing 30 actin filaments (red) and 1000 bivalent crosslinkers (green spheres). Please refer to the Supplemental Methods section for a detailed description of the model. Actin-binding kinetics were chosen from previous simulations (**Fig. 4I**) to correspond to ring-forming conditions for bivalent crosslinkers. The elongation rate at the plus (+) end is constant at 0.0103 μm/s, and neither end undergoes monomer disassociation. **B)** Increasing the simulation time to 2400 s recovers ring formation in a viscosity condition where rings are absent at 600 s. Representative final snapshots (t = 2400 s) from multiple replicates ($N_{replicates}$ = 5) of systems with viscosity = 5.0 Pa·s within spherical condensates (R = 1 μm) containing 30 actin filaments (red) and 1000 bivalent crosslinkers (green spheres). Please refer to the Supplemental Methods section for a detailed description of the model. Actin-binding kinetics were chosen from previous simulations (**Fig. 4I**) to correspond to ring-forming conditions for bivalent crosslinkers. The elongation rate at the plus (+) end is constant at 0.0103 μm/s, and neither end undergoes monomer disassociation. **C-E: Simulations show that increasing the number of bivalent crosslinkers in the system from the 1000 used elsewhere has little effect on the resulting actin structure. C)** Representative final snapshots (t = 600 s) from simulations at various binding and unbinding rates within spherical condensates (R = 1 μm) containing 30 actin filaments (red) and different numbers of bivalent crosslinkers (green spheres). Please refer to the Supplemental Methods section for a detailed description of the model. The binding rate of the bivalent crosslinkers to actin is held constant at 1.0 s^{-1} in all simulation conditions. The number of bivalent crosslinkers simulated is varied along each column, and unbinding rates are varied along each row. The elongation rate at the plus (+) end is constant at 0.0103 μm/s, and neither end undergoes monomer disassociation. **D)** Representative final snapshots shown in **C** showing just the actin filaments in red. **E)** Stacked bar graph showing the distribution of condensate protein at different states namely, free monomers, free dimers, actin-bound monomers, and actin-bound dimers. Error bars show standard deviation. Data used: 5 replicates, data from last 30 snapshots.

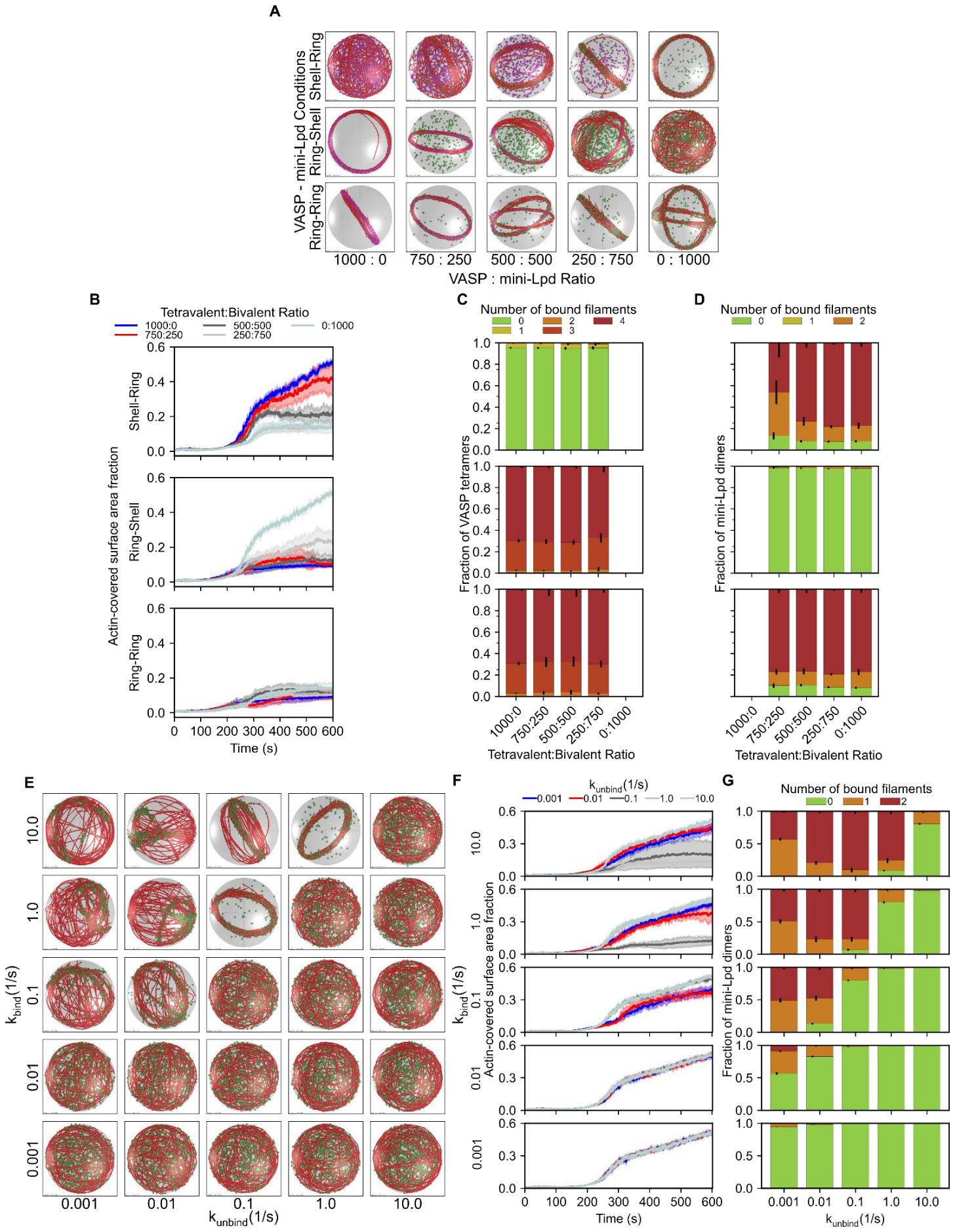
A
VASP - mini-Lpd Conditions
Shell-Ring
Ring-Shell
Ring-Ring
1000 : 0
750 : 250
500 : 500
250 : 750
0 : 1000
VASP : mini-Lpd Ratio
B
Tetravalent:Bivalent Ratio
1000:0
750:250
500:500
250:750
0:1000
Shell-Ring
Ring-Shell
Ring-Ring
Actin-covered surface area fraction
Time (s)
C
Number of bound filaments
Fraction of VASP tetramers
Tetravalent:Bivalent Ratio
D
Number of bound filaments
Fraction of mini-Lpd dimers
Tetravalent:Bivalent Ratio
E
k_bind(1/s)
k_unbind(1/s)
F
k_unbind(1/s)
0.001
0.01
0.1
1.0
10.0
Actin-covered surface area fraction
Time (s)
G
Number of bound filaments
Fraction of mini-Lpd dimers
k_unbind(1/s)

Figure S6: Simulations show that ring and shell-shaped actin network structures are conserved within condensates of mini-Lpd and VASP of various mole ratios. Related to Figures 3-5. A) Representative final snapshots (t = 600 s) from simulations for three different crosslinker kinetic conditions at various VASP to mini-Lpd mole ratios. Condensates are spherical (R = 1 μm), contain 30 actin filaments (red), and a total of 1000 crosslinkers (tetravalent crosslinkers in purple and bivalent crosslinkers in green). Please refer to the Supplemental Methods section for a detailed description of the model. Ring-forming kinetics (k_{bind} = 10.0 s^{-1}, k_{unbind} = 1.0 s^{-1}) or shell-forming kinetics (k_{bind} = 0.1 s^{-1}, k_{unbind} = 1.0 s^{-1}) are the same for both types of crosslinkers. The elongation rate at the plus (+) end is constant at 0.0103 μm/s, and neither end undergoes monomer disassociation. See **Video S1** for a video of representative trajectories. **B-D**: Analysis metrics used to understand actin organization within condensates at various number ratios of tetravalent and bivalent crosslinkers. **B)** Mean (solid line) and standard deviation (shaded area) of the condensate surface area covered with actin is shown as a time series. Time series is colored by tetravalent: bivalent ratio. Each subpanel shows simulations for the different actin-binding parameters used. For example, Shell-Ring corresponds to kinetic parameter choice where we have observed shell formation with 1000 molecules of tetravalent crosslinker and ring formation when simulated with 1000 molecules of bivalent crosslinker respectively. **C)** The stacked bar graphs show the distribution of tetravalent crosslinkers (VASP) molecules among various allowed valency states (mentioned above) as we change the copy number ratio. Error bars represent standard deviation. **D)** The stacked bar graphs show the distribution of bivalent crosslinkers (mini-Lpd) molecules among various allowed valency states (mentioned above) as we change the copy number ratio. Error bars represent standard deviation. Data used: 5 replicates per kinetic condition (namely, Shell-Ring, Ring-shell, and Ring-Ring), bar graphs generated with data from the last 30 snapshots from each of the replicates. **E)** Simulations show that mini-Lpd kinetics affect actin network organization in liquid-liquid phase-separated mini-Lpd dimer condensates. Representative final snapshots (t = 600 s) from simulations at various binding and unbinding rates within spherical condensates (R = 1 μm) containing 30 actin filaments (red) and 1000 bivalent crosslinkers (green). Please refer to the Supplemental Methods section for a detailed description of the model. The binding rates of the bivalent crosslinkers are varied along each column, and unbinding rates are varied along each row. The elongation rate at the plus (+) end is constant at 0.0103 μm/s, and neither end undergoes monomer disassociation. Also, see **Video S3**. **F-G: Kinetics of the actin-covered surface area fraction time series and the fraction of mini-Lpd bound to zero, one, and two actin filaments.** The mini-Lpd binding rate is changed across the panels (shown on the left side of the figure). **F)** The mini-Lpd unbinding rate is varied and displayed as a time series of the actin-covered surface area fraction. **G)** Stacked bar graphs representing the fraction of bivalent crosslinkers bound to 0, 1, or 2 actin filaments for each condition. The error bars represent the standard deviation. Ten replicates are considered per condition, and the data was obtained from the last 30 snapshots (5%) of each replicate.

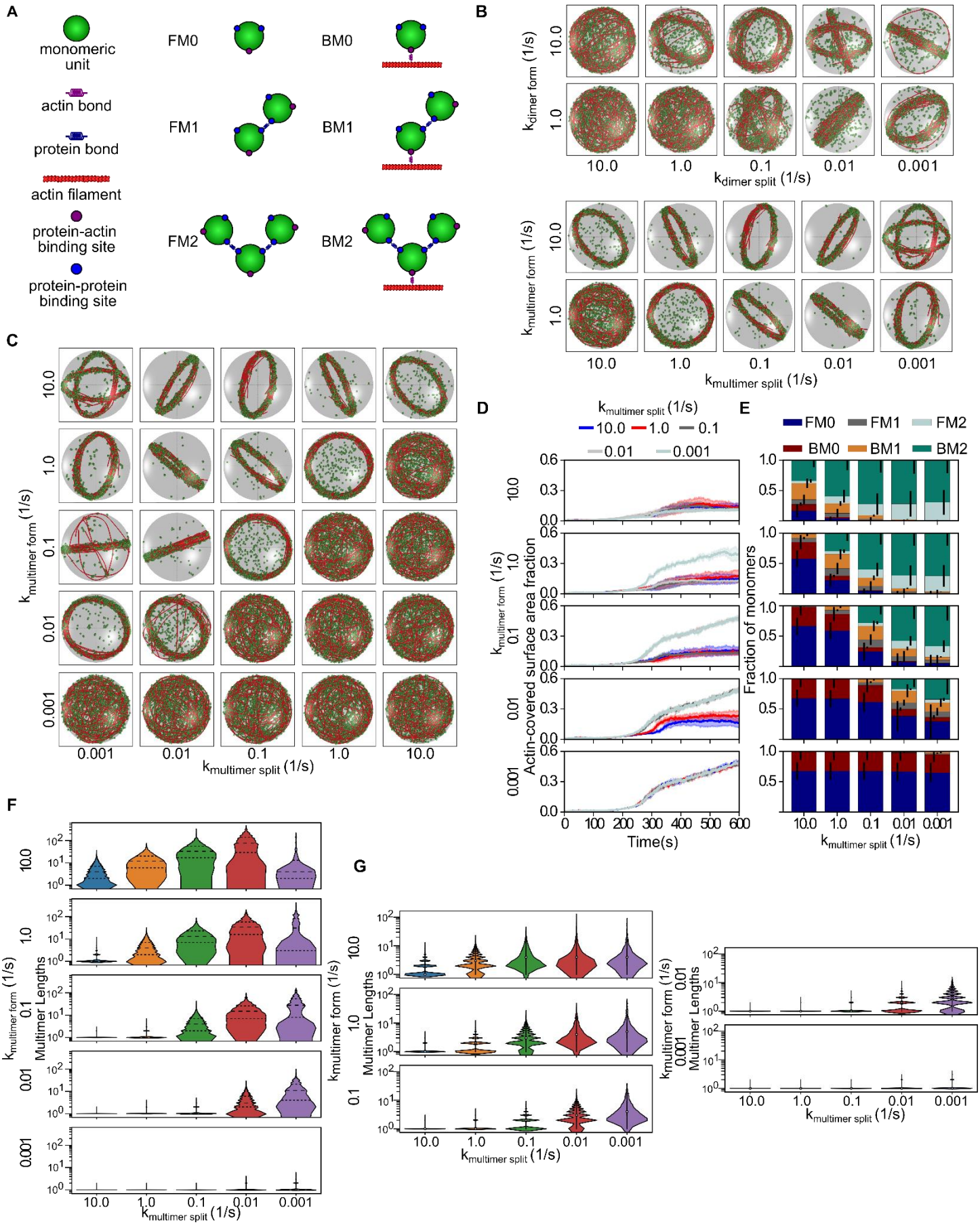
A
monomeric unit
actin bond
protein bond
actin filament
protein-actin binding site
protein-protein binding site
FM0
BM0
FM1
BM1
FM2
BM2
B
k_dimer form (1/s)
k_dimer split (1/s)
k_multimer form (1/s)
k_multimer split (1/s)
10.0
1.0
0.1
0.01
0.001
C
k_multimer form (1/s)
k_multimer split (1/s)
D
k_multimer split (1/s)
10.0 1.0 0.1 0.01 0.001
Actin-covered surface area fraction
Time(s)
E
FM0 FM1 FM2
BM0 BM1 BM2
Fraction of monomers
F
Multimer Lengths
k_multimer form (1/s)
k_multimer split (1/s)
G
Multimer Lengths
k_multimer form (1/s)
k_multimer split (1/s)

Figure S7: Lpd-mimics that can multimerize dynamically bundle actin more robustly than monomers limited to dynamic dimerization. Related to Figure 5. A) Schematic depicting the potential configurations quantified for the dynamic multimerization model. BM (Bound Monomer) refers to monomeric units that are bound to an actin filament while FM (Free Monomer) refers to those that are not; the corresponding number (0, 1, or 2) indicates the number of other monomers that a single monomeric unit is bound to. **B)** Side-by-side comparison of the representative final snapshots (t = 600 s) from simulations of the (top) dynamic dimerization and (bottom) dynamic multimerization models. These simulations detail various multimer formation and splitting rates within spherical condensates (R = 1 μm) containing 30 actin filaments (red) and 2000 monomers (green spheres) which can form either A) only dimers or B) multimers of various lengths. Please refer to the Supplemental Methods section for a detailed description of the models. The monomer-monomer binding rates are varied along each column, and monomer-monomer splitting rates are varied along each row. Actin-binding kinetics were chosen from previous simulations shown in **Fig. 4I** to correspond to ring-forming conditions for bivalent crosslinkers. The elongation rate at the plus (+) end is constant at 0.0103 μm/s, and neither end undergoes monomer disassociation. **C)** Representative final snapshots (t = 600 s) from simulations at various multimer formation and splitting rates within spherical condensates (R = 1 μm) containing 30 actin filaments (red) and 2000 monomers (green spheres) which can form multimers of various lengths. Please refer to the Supplemental Methods section for a detailed model description. The monomer-monomer binding rates are varied along each column, and monomer-monomer splitting rates are varied along each row. Actin-binding kinetics were chosen from previous simulations shown in **Fig. 4I** and are consistent with simulations in **Fig. 5B** to favor ring formation. The elongation rate at the plus (+) end is constant at 0.0103 μm/s, and neither end undergoes monomer disassociation. **D)** Time series showing the mean (solid line) and standard deviation (shaded area) of simulated condensate surface that is covered with actin. The $k_{multimer\text{-}form}$ value is shown on top of each subpanel while time series are colored by $k_{multimer\text{-}split}$ values. Data used: 5 replicates. Please refer to the Supplemental Methods section for a detailed description. **E)** A stacked bar graph showing the distribution of condensate protein in different states. BM (Bound Monomer) refers to monomeric units that are bound to an actin filament while FM (Free Monomer) refers to those that are not; the corresponding number (0, 1, or 2) indicates the number of other monomers that a single monomeric unit is bound to. Please note that we refer to the condensate-forming protein as monomers. Error bars show standard deviation. Data used: 5 replicates, data from last 30 snapshots. **F-G**: Violin plots showing the distribution of multimer lengths for each simulation condition for systems **F)** with actin filaments and **G)** without actin filaments. Larger multimer lengths are observed in the presence of actin filaments. Lengths are counted as the number of monomers that constitute a single multimer chain. Violin plot densities are normalized such that all plots are fit to the same width. Data used: 5 replicates, data from last 30 snapshots.

Methods S1: Characteristics of the agent-based model used for experiments. Related to Fig. 3-6 and STAR Methods.

Chemical and mechanical framework employed in Cytosim

Simulations were performed in Cytosim (https://gitlab.com/f-nedelec/cytosim), an agent-based modeling framework which simulates the chemical dynamics and mechanical properties of filament networks. Cytosim models filament dynamics and diffusing species by numerically solving a constrained Langevin framework in a viscous medium at short time intervals. Actin filaments are represented as inextensible fibers composed of a series of linear segments of length 100 nm connected at hinge points to allow for bending. Cytosim computes the bending energy of the fiber using the specified flexural rigidity in the input parameters. In this study, cross-linking molecules (mini-Lpd, VASP, mini-Lpd monomers) are modeled as spherical solids of radius 30 nm with a specified number and type of binding sites corresponding with the class of molecule (**Fig. S4**). The binding distance specifies the radius within which the concentration of the corresponding reactant is considered as part of the binding reaction. The unbinding rate specifies the rate constant used in a Bell's law model representation of slip bond unbinding kinetics. We started with the simulation framework in our previous work[S4,10]. We assumed that only a subset of crosslinking molecules participate in bundling owing to steric accessibility issues. The condensate was represented by a spherical volume of radius 1.0 μm with a rigid, repulsive boundary. We considered 30 actin filaments within the condensate, each of length 0.1 μm. The actin filament elongation rate is 0.0103 μm/s, calculated assuming a final filament length of 2π μm. The simulation run time is 600 s and was informed by experiments. Please refer to Table S1 for a detailed description of the parameters used in the model and Table S2 for a detailed description of simulation specific parameters varied. In this study, we performed simulations by modeling mini-Lpd molecules as solids with two binding sites (**Fig. S4** and **Fig. 4**) and VASP molecules as solids with four actin-binding sites (**Fig. S4**). Additionally, we also modified the codebase to model mini-Lpd molecules as those that dimerize based on a given formation and splitting rates.

Position evolution

Cytosim uses the Langevin equation to calculate the evolution of discretized points over time, thus describing the 3D position of each actin filament and crosslinking molecule in the system at each time step for the duration of the simulation. In a 3D system of N particles, there are a total of 3N coordinates where each particle i has its coordinates given by $x_i = \{x_{i1}, x_{i2}, x_{i3}\}$. Each particle's position x_i is then evolved along each dimension j as governed by the following stochastic differential equation:

$$dx^{ij}(t) = \mu f_{tot}^{ij}(t)dt + dB_j(t)$$

Here, μ is the viscosity of the solvent, $f^{ij}_{tot}(t)$ is the total force acting on each particle as a function of time, and $B_j(t)$ is the diffusion (noise) term. The noise term is given by a randomly sampled variable from a normal distribution centered around a mean of 0 with a standard deviation of $\sqrt{2D^i dt}$. The diffusion constant D is given by the Einstein relation $D = \mu k_B T$ where k_B is the Boltzmann constant and T is temperature.

Steric considerations

It is important to consider steric repulsion potentials to prevent spatial overlap of molecules. Additionally, crowding also affects the effective mobility of molecules thereby altering the propensities of chemical reactions in our system. As such, we employ a steric repulsion potential between the diffusing elements in our simulations, the crosslinking molecules, and actin filaments.

Actin-droplet kinetics

To understand how actin-droplet affinity leads to filament bundling, we model crosslinking reactions between actin and droplet molecules. The binding rate used in this study is specified in **Table S1**. The stochastic mesoscopic rates (k_{bind}) employed in the simulations are related to second-order binding rates ($k_{bind,2}$) with units of molarity as follows.

$k_{bind,2}/(N_{AV} \times V_{bind}) = k_{bind}$,

Where, N_{AV} is the Avogadro number and represents the V_{bind} binding volume. Molecules within the binding volume alone can stochastically bind actin. The binding volume is a cylinder of radius given by the binding distance (r_{bind}) and height given by the length of the actin segment (100 nm, **Table S1**).

The unbinding rate (k_{unbind}) is force-sensitive and given by k_{unbind}=$k_{unbind}{}^{0} exp(F/F_{unbind})$, where $k_{unbind}{}^{0}$ is the zero-force unbinding rate, F is the force experienced by the actin-droplet molecule bond and F_{unbind} represents the unbinding force. Binding affinity (as shown in **Figure 5B**) can be calculated from $K_d = k_{unbind}/k_{bind}$.

Dynamic dimerization and dynamic multimerization models

As the mini-Lpd molecules bundle actin even in the absence of a leucine zipper, we hypothesized that the interaction between mini-Lpd could be sufficient to form multimers. We begin by simulating molecules capable of dynamic dimerization. The dynamic dimerization model simulates independently diffusing monomers as solids that each have a single actin-binding site and a single dimerization site capable of binding to another monomer to dynamically form dimers. Each monomer-monomer binding site mimics the favorable enthalpic interactions between mini-Lpd monomers in the absence of a leucine zipper domain. This model introduces new input parameters that describe the kinetics of forming and splitting dimers and differs from the other simulations where bivalent crosslinkers are prescribed as a single solid representing a static dimer with two binding sites. The implementation of our dynamic dimerization model required edits to the Cytosim source code to simulate dimerization reactions. The binding and unbinding reactions are modeled similarly to Actin-droplet interactions. The corresponding binding volume is given by a sphere with radius as the corresponding binding distance. Please refer to **Table S1** for a detailed description of the parameter values considered.
Further, we also explore the role of multivalency by simulating droplets with molecules that can interact with up to two other molecules in the dynamic multimerization model. As a result, we allow for the formation of higher multimeric states such as trimers, tetramer, etc. These source code edits are available on the GitHub repository available with this publication.

Limitations of the model

Our proposed model for dynamic dimerization represents molecules as spheres. As a result, we do not explore the role of entanglement-driven reptation of polymeric condensate molecules in controlling droplet dynamics.[S11] Further, the multivalent interactions that happen along the chain are coarse-grained as binding/unbinding reactions. Modeling efforts using associative polymers (sticker-spacer models) consider the sticker-sticker interaction energies in the range of 1-10 k_BT to ensure stable droplet formation.[S12,13] Such efforts will be explored in the future to understand the role that polymer chain entropy and multivalency play in controlling reactions within the droplet.

Actin-covered surface area calculation

At the end of the simulation time, each actin filament grows to approach the length of the circumference of the spherical condensate. At this point, each actin filament will lie primarily at or near the condensate surface (defined with a threshold distance from the boundary of 100 nm). By discretizing the surface of the condensate to an icosphere and each actin filament into discrete monomers, the surface density at each time point in our simulation is obtained via the fraction of occupied triangles on the icosphere. The icosphere was generated by dividing the initial eight triangles 3 more times to generate triangles whose effective size was comparable to 10 actin monomers.[S4]

Supplemental References

S1. Wang, H., Kelley, F.M., Milovanovic, D., Schuster, B.S., and Shi, Z. (2021). Surface tension and viscosity of protein condensates quantified by micropipette aspiration. Biophys. Rep. *1*, 100011. https://doi.org/10.1016/j.bpr.2021.100011.

S2. Mogilner, A., and Oster, G. (1996). Cell motility driven by actin polymerization. Biophys. J. *71*, 3030. https://doi.org/10.1016/S0006-3495(96)79496-1.

S3. Gittes, F., Mickey, B., Nettleton, J., and Howard, J. (1993). Flexural rigidity of microtubules and actin filaments measured from thermal fluctuations in shape. J. Cell Biol. *120*, 923–934. https://doi.org/10.1083/jcb.120.4.923.

S4. Chandrasekaran, A., Graham, K., Stachowiak, J.C., and Rangamani, P. (2024). Kinetic trapping organizes actin filaments within liquid-like protein droplets. Nat. Commun. *15*, 3139. https://doi.org/10.1038/s41467-024-46726-6.

S5. Ferrer, J.M., Lee, H., Chen, J., Pelz, B., Nakamura, F., Kamm, R.D., and Lang, M.J. (2008). Measuring molecular rupture forces between single actin filaments and actin-binding proteins. Proc. Natl. Acad. Sci. *105*, 9221–9226. https://doi.org/10.1073/pnas.0706124105.

S6. Lotthammer, J.M., Ginell, G.M., Griffith, D., Emenecker, R.J., and Holehouse, A.S. (2024). Direct prediction of intrinsically disordered protein conformational properties from sequence. Nat. Methods *21*, 465–476. https://doi.org/10.1038/s41592-023-02159-5.

S7. Joseph, J.A., Reinhardt, A., Aguirre, A., Chew, P.Y., Russell, K.O., Espinosa, J.R., Garaizar, A., and Collepardo-Guevara, R. (2021). Physics-driven coarse-grained model for biomolecular phase separation with near-quantitative accuracy. Nat. Comput. Sci. *1*, 732–743. https://doi.org/10.1038/s43588-021-00155-3.

S8. Chu, X., Sun, T., Li, Q., Xu, Y., Zhang, Z., Lai, L., and Pei, J. (2022). Prediction of liquid–liquid phase separating proteins using machine learning. BMC Bioinformatics *23*, 72. https://doi.org/10.1186/s12859-022-04599-w.

S9. Chen, Z. (2021). Networks of interacting proteins contribute to membrane curvature sensing. Biophys. J. *120*, 752–753. https://doi.org/10.1016/j.bpj.2021.01.023.

S10. Graham, K., Chandrasekaran, A., Wang, L., Yang, N., Lafer, E.M., Rangamani, P., and Stachowiak, J.C. (2024). Liquid-like condensates mediate competition between actin branching and bundling. Proc. Natl. Acad. Sci. *121*, e2309152121. https://doi.org/10.1073/pnas.2309152121.

S11. Kolinski, A., Skolnick, J., and Yaris, R. (1987). Does reptation describe the dynamics of entangled, finite length polymer systems? A model simulation. J. Chem. Phys. *86*, 1567–1585. https://doi.org/10.1063/1.452196.

S12. Ranganathan, S., and Shakhnovich, E.I. (2020). Dynamic metastable long-living droplets formed by sticker-spacer proteins. eLife *9*, e56159. https://doi.org/10.7554/eLife.56159.

S13. Chattaraj, A., and Shakhnovich, E.I. (2024). Separation of sticker-spacer energetics governs the coalescence of metastable biomolecular condensates. bioRxiv, 2023.10.03.560747. https://doi.org/10.1101/2023.10.03.560747.